BLTP3A is associated with membranes of the late endocytic pathway and is an effector of CASM

Short title: BLTP3A: a late endocytic factor and CASM effector

Michael G. Hanna[1-5], Hely O. Rodriguez Cruz[1-5], Kenshiro Fujise[1-5], Yumei Wu[1-5], C. Shan Xu[6], Song Pang[7], Zhuonging Li[8], Mara Monetti[8], Pietro De Camilli*[1-5]

[1]Department of Neuroscience, Yale University School of Medicine, New Haven, CT;

[2]Department of Cell Biology, Yale University School of Medicine, New Haven, CT;

[3]Howard Hughes Medical Institute, Yale University School of Medicine, New Haven, CT;

[4]Program in Cellular Neuroscience, Neurodegeneration and Repair, Yale University School of Medicine, New Haven, CT;

[5]Aligning Science Across Parkinson's (ASAP) Collaborative Research Network, Chevy Chase, MD;

[6]Department of Cellular and Molecular Physiology, Yale University School of Medicine, New Haven, CT;

[7]Yale University School of Medicine, New Haven, CT;

[8]Proteomics Core Facility, Sloan Kettering Institute, Memorial Sloan Kettering Cancer Center, New York, NY.

*Correspondence to Pietro De Camilli: pietro.decamilli@yale.edu

Keywords

Bridge-like lipid transfer protein, BLTP, BLTP3A, BLTP3B, Rab7, lysosome, lysosomal membrane damage, CASM, mATG8, LLOMe, Rab45

Teaser

BLTP3A is localized on membranes of the late endocytic system and is CASM effector, pointing to a role of this proteins in the response to lysosome damage

ABSTRACT

Recent studies have identified a family of rod-shaped proteins thought to mediate lipid transfer at intracellular membrane contacts by a bridge-like mechanism. We show one such protein, bridge-like lipid transfer protein 3A (BLTP3A)/UHRF1BP1 binds VAMP7 vesicles via its C-terminal region and anchors them to lysosomes via its chorein domain containing N-terminal region to Rab7. Upon lysosome damage, BLTP3A-positive vesicles rapidly (within minutes) dissociate from lysosomes. Lysosome damage is known to activate the CASM (Conjugation of ATG8 to Single Membranes) pathway leading to lipidation and recruitment to lysosomes of mammalian ATG8 (mATG8) proteins. We find that this process drives the reassociation of BLTP3A with damaged lysosomes via an interaction of its LIR motif with mATG8 which coincides with a dissociation from the vesicles. Our findings reveal that BLTP3A is an effector of CASM, potentially as part of a mechanism to help repair or minimize lysosome damage.

INTRODUCTION

Eukaryotic cells are populated by anatomically discontinuous lipid-based intracellular membranes and thus require mechanisms to transfer lipids between them. This is achieved both by membrane traffic (Palade, 1975) and by lipid transfer proteins (LTPs) (DeGrella and Simoni, 1982; Wirtz, 1991; Reinisch et al., 2024) or protein complexes that have the property to extract lipid from membranes, shield them in hydrophobic cavities and insert them into acceptor membranes. Typically, LTPs function at sites where two membranes are closely apposed, i.e. where transfer may occur with greater speed and specificity (Saheki and Camilli, 2017; Cohen et al., 2018; Scorrano et al., 2019; Wong et al., 2019; Prinz et al., 2020; Voeltz et al., 2024). Moreover, in most cases studied so far transfer occurs via a shuttle mechanism in which a lipid harboring module that contains one or few lipids, is connected via flexible linkers to protein domains that tether the two membranes together (Prinz et al., 2020; Reinisch et al., 2024). In recent years, however, the occurrence of an additional mode of lipid transfer, mediated by rod-like proteins that harbor a hydrophobic groove or tunnel along which lipids can slide and which directly bridge two membranes has been described (Kumar et al., 2018; Osawa et al., 2019; Maeda et al., 2019; Valverde et al., 2019; Wong et al., 2019; Li et al., 2020; Leonzino et al., 2021; Dziurdzik and Conibear, 2021; Cai et al., 2022a; Hanna et al., 2022; Adlakha et al., 2022; Kang et al., 2024; Banerjee et al., 2024). These proteins, collectively referred to as bridge-like lipid transfer proteins (BLTPs), are evolutionary related and have a similar basic molecular architecture (Leonzino et al., 2021; Neuman et al., 2022; Levine, 2022; Hanna et al., 2023). Their core is represented by concatemers of small beta-sheets with a taco-like fold, referred to as repeating beta-groove (RBG) modules (Levine, 2022; Hanna et al., 2023), which are lined by hydrophobic amino acids (a.a.) at their inner surface, thus generating a continuous hydrophobic surface (Kumar et al., 2018; Li et al., 2020; Levine, 2022; Neuman et al., 2022; Hanna et al., 2023; Kang et al., 2024; Wang et al., 2024b). Moreover, they comprise motifs or domains that allow them to tether two different membranes and a variety of loops or outpocketings of variable length which may have regulatory or protein-protein interaction functions (Kumar et al., 2018; Dziurdzik and Conibear, 2021; Guillén-Samander et al., 2021; Neuman et al., 2022; Adlakha et al., 2022; Guillén-Samander et al., 2022; van Vliet et al., 2022; Hanna et al., 2023; Kang et al., 2024; Wang et al., 2024a; b). They are thought to mediate bulk lipid (generally phospholipid) transfer between membranes. As the groove at its narrowest point can only accommodate one phospholipid, such transport is thought to be unidirectional (Li et al., 2020; Kang et al., 2024; Wang et al., 2024b). BLTPs comprise VPS13, the founding member of the family, as well as the autophagy factor ATG2, and other proteins originally referred to by multiple different names in different organisms and are now renamed BLTP1, BLTP2 and BLTP3 (Neuman et al., 2022; Hanna et al., 2023). These proteins differ in the number of RBG modules and thus in length: 17 in BLTP1, the longer member of the family and six in BLTP3, the shorter family member (Levine, 2022).

The putative role of BLTPs in bulk lipid transfer is ideally suited for membrane bilayer expansion or repair via the delivery of newly synthesized lipids from the ER, a possibility strongly supported by the well-established roles of yeast VPS13 in the growth of the sporulation membrane (Park and Neiman, 2012) and of ATG2 in the expansion of the isolation membrane (Wang et al., 2001; Velikkakath et al., 2012; Gómez-Sánchez et al., 2018; Osawa et al., 2019; Valverde et al., 2019).

Other processes in which BLTPs anchored to the ER have been implicated also involve membrane expansion, such as biogenesis of mitochondria and of peroxisomes (Park et al., 2016; John Peter et al., 2017; Anding et al., 2018; Baldwin et al., 2021; Guillén-Samander et al., 2021), organelles not connected to the ER by membrane traffic. In other cases, the relation of the putative bulk lipid transfer function of BLTPs to bilayer expansion is less clear, and BLTPs seem to be primarily important to control the composition of the receiving bilayer (Tokai et al., 2000; John Peter et al., 2022; Wang et al., 2022; Hanna et al., 2022; Banerjee et al., 2024). In this case delivery of new lipids to a membrane may be removed by a compensatory mechanism, for example by membrane traffic, thereby limiting expansion overall. As BLTPs have been identified only recently, much remains to be discovered about their function.

Two very similar BLTPs of which little is known are BLTP3A (also called UHRF1BP1) and BLTP3B (also called SHIP164 or UHRF1BP1L for UHRF1BP1-Like) (Hanna et al., 2022; Neuman et al., 2022). BLTP3A was originally identified as a Binding Protein (BP) of the epigenetic regulator UHRF1 (Unoki et al., 2004) while its paralogue BLTP3B was independently identified as an interactor of syntaxin 6 (Syntaxin 6 Habc-interacting protein of 164 kDa, hence its alias SHIP164) and found to localize on membrane of the endocytic pathway harboring this SNARE protein (Otto et al., 2010). BLTP3A and BLTP3B were also top hits in a screen for effectors of Rab7 and Rab5, respectively (Gillingham et al., 2019).

Following up on these earlier studies we have recently reported a systematic characterization of the properties of BLTP3B (Hanna et al., 2022). We showed that endogenous BLTP3B is localized on clusters of endocytic vesicles that interact with components of the retrograde microtubule-based transport system [dynein light chain (DYNLL1/2)] (Carter et al., 2016) and Rab45 (CRACR2a) (Wang et al., 2019) and that loss of BLTP3B results in a perturbation of the retrograde traffic to the Golgi area of the cation independent mannose-6-phosphate receptor (MPR) (Lin et al., 2003). Exogenous expression of BLTP3B, leading to its overexpression, resulted in a striking accumulation of these vesicles that formed tightly packed clusters anchored to Rab5-positive early endosomes (Hanna et al., 2022). How the putative lipid transfer function of BLTP3B relate to this localization and phenotypes remains an open question.

The goal of the present study was to acquire new information about BLTP3A, a risk gene for lupus erythematosus (Gateva et al., 2009; Zhang et al., 2011; Wen et al., 2020). We report here that BLTP3A, like BLTP3B, is localized on clusters of small vesicles and that its overexpression induces a massive expansion of such clusters. However, while clusters of BLTP3B-positive vesicles are anchored to Rab5-positive organelles, clusters of BLTP3A-positive vesicles are anchored to LAMP1-positive organelles via Rab7. We further show that lysosome damage triggers the rapid loss of the Rab7-dependent association of BLTP3A with LAMP1-positive organelles, followed by its CASM (Durgan and Florey, 2022)-dependent reassociation with them in an mATG8 and LIR motif-dependent way. These findings have implications for lysosome health, as perturbation of their membranes reveals a faster lysis in BLTP3A KO cells than in control cells. Collectively, our results point to a role of this protein at the interface between late endocytic traffic and lysosomes and also raise the possibility that BLTP3A may play a role in the response to lysosome damage.

RESULTS

Close structural similarity, but different interactions, of BLTP3A relative to BLTP3B

BLTP3A is very similar to BLTP3B (41% identity and 58% positives in primary sequence). Moreover, fold-prediction algorithms (Jumper et al., 2021; Yang et al., 2020) show that BLTP3A shares all the key structural features of BLTP3B: a rod-like core composed by six RBG motifs (Levine, 2022), a hydrophobic groove that runs along its entire length, a large disordered outpocketing of the rod-like core (a.a. 885-1188) and a C-terminal helix (a.a. 1394-1440) (**Figure 1A**). Both BLTP3A and BLTP3B are reported in Biogrid (https://thebiogrid.org) to be interactors of Rab45 (CRACR2a), an adaptor for dynein and retrograde microtubule traffic (Wang et al., 2019) and, accordingly, over-expression of GFP-Rab45 in RPE-1 cells concentrated BLTP3A-mRFP to perinuclear spots (the centrosomal area) similar to our previous findings of BLTP3B (**Supplemental Figure 1A**) (Hanna et al., 2022). Despite these similarities, BLTP3A lacks the motifs responsible for binding to syntaxin-6 (Stx6) and the dynein light chain (DYNLL1/2) (**Figure 1B**), which we had identified in BLTP3B (Hanna et al., 2022). Moreover, BLTP3A was shown to be an effector of Rab7, instead of Rab5 (Gillingham et al., 2019). A per-residue evolutionary conservation analysis of BLTP3A carried out using the ConSurf server (Armon et al., 2001; Yariv et al., 2023) revealed that most conserved residues belong to the RBG motif core, particularly its N-terminal portion (**Figure 1A**). Short stretches of conserved residues, however, are also present in predicted unfolded loops emerging from this core, including the large outpocketing. As revealed by western blotting, BLTP3A, like BLTP3B, has broad expression in different mouse tissues (**Figure 1C**), with higher levels occurring in brain and lung.

BLTP3A localizes to foci concentrated near lysosomes

In a previous preliminary analysis of BLTP3A localization (Hanna et al., 2022) we had shown that exogenously expressed fluorescently tagged BLTP3A appears as fluorescent foci localized in proximity of organelles positive for the lysosome marker LAMP1 and of Rab7, a Rab associated with late endosome and lysosomes (these organelles will be referred to henceforth collectively as “lysosomes”). As our study of BLTP3B had shown that its exogenous expression resulted in an enlargement of the BLTP3B positive compartment (vesicle clusters), we wished to confirm that even endogenous BLTP3A was localized in proximity of lysosomes. Available antibodies directed against BLTP3A did not detect a clear specific signal by immunocytochemistry. Thus, we turned to a knock-in strategy to epitope tag the endogenous protein. Since preliminary experiments revealed heterogeneity in the expression levels of BLTP3A in frequently used cell lines, we chose A549 cells (lung adenocarcinoma epithelial cells) for these experiments where we detected robust expression of BLTP3A, consistent with high expression of BLTP3A in the lung (**Figure 1C**).

The BLTP3A locus in A549 cells was edited by inserting after residue V904 a nucleotide sequence encoding a single V5 epitope flanked on either side with short GSGSG linkers (**Supplemental Figure 1B**). This site is within a predicted disordered region and is not expected to change the lipid channel core of BLTP3A **(Supplemental Figure 1C).** Edited BLTP3A was validated by

Western blotting of homogenates of edited cells revealing a V5-positive band (endogenous BLTP3A^V5) with the same motility as BLTP3A (**Figure 1D**).

Anti-V5 immunofluorescence of edited cells showed small weakly fluorescence puncta throughout the cytoplasm, which were enriched in central regions of cells (**Figure 1E**) and were not observed in WT cells immunostained under the same conditions (**Figure 1E**). Importantly, many V5-positive puncta were adjacent to, or partially overlapping with, the fluorescence produced by antibodies against LAMP1 (**Figure 1E**), consistent with BLTP3A being a Rab7 effector. The fluorescence of exogenously expressed tagged BLTP3A-GFP overlapped with anti-V5 immunofluorescence of edited cells, in agreement with our previous preliminary findings (Hanna et al., 2022), although accumulations of BLTP3A-GFP fluorescence were much larger (**Figure 1E**).

Large BLTP3A foci produced by BLTP3A overexpression represent clusters of vesicles anchored to lysosomes

Given the similar localization of endogenous and exogenous BLTP3A next to lysosomes, we capitalized on exogenous BLTP3A tagged with various fluorescently tagged proteins, i.e. constructs which could be analyzed by Correlative Light-Electron Microscopy (CLEM) (immunofluorescence of the V5 epitope requires fixation and permeabilization, i.e. a treatment that perturbs cell ultrastructure). We primarily used RPE-1 cells for these studies, as LAMP1-positive organelles in these cells are very large, abundant, clustered around the Golgi complex and nucleus (**Figure 1F**), and thus easy to identify by microscopy even without specific markers. Upon co-expression of LAMP1-GFP and BLTP3A-mRFP (**Figure 1G**), two sets of BLTP3A-mRFP-positive structures were observed by fluorescence microscopy: i) BLTP3A-mRFP accumulations directly adjacent to lysosomes, often bridging two closely apposed LAMP1-GFP-vacuoles and ii) larger (often very large) BLTP3A-mRFP accumulations not obviously connected to the large LAMP1-GFP-vacuoles. Analysis of these structures by CLEM in RPE-1 cells also expressing mito-BFP (to help fluorescence - EM alignment) showed that BLTP3A-mRFP foci represented tightly packed clusters of approximately 50-70 nm vesicles (**Figure 1H**). Importantly, the vesicles of such clusters directly adjacent to LAMP1-GFP vacuoles appeared to be tethered to lysosomal membranes, with an average distance of ~10-11 nm (**Figure 1I**).

This exaggerated accumulation of large clusters of small vesicles mirrors what we had observed upon overexpression of BLTP3B, indicating that a shared property of BLTP3A and BLTP3B is to bind small vesicles, induce their accumulation, cluster them, and anchor such clusters to other organelles–although clusters of BLTP3B vesicles are anchored to early endosomes (consistent with BLTP3B being an effector of Rab5), while clusters of BLTP3A are anchored to late endosomes/lysosomes (consistent with BLTP3A being an effector of Rab7). As our study of BLTP3B had shown that even BLTP3B expressed at an endogenous level is localized to vesicle clusters which are much smaller than clusters observed upon BLTP3B overexpression (Hanna et al., 2022), we hypothesized that the massive accumulation of vesicles observed upon overexpression of BLTP3 isoforms reflect a property of these proteins to nucleate biomolecular condensates. Accordingly, live imaging revealed that both clusters of BLTP3A and of BLTP3B

(see Video 1 and Figure 8E from Hanna et al., 2022) are highly dynamic. For example, they can undergo fission into smaller clusters, as expected for a compartment with liquid-like properties.

BLTP3A positive vesicles contain VAMP7, a SNARE implicated in traffic to lysosomes

The clustering of BLTP3A-positive vesicles next to lysosomes suggested that they may represent organelles destined to fuse with them, perhaps arrested at a docking stage due to a dominant negative effect of BLTP3A overexpression. As at least some of the vesicles that fuse with late endosomes and lysosomes harbor VAMP7 in their membrane (Advani et al., 1999; Pols et al., 2013), we explored the potential presence of this SNARE in BLTP3A-positive vesicles (**Figure 1J**). Supporting this hypothesis, anti-VAMP7 immunofluorescence revealed a striking overlap with the fluorescence of BLTP3A-mRFP both on the isolated BLTP3A clusters and on those anchored to lysosomes (**Figure 1J**). A similar overlap was observed between the BLTP3A signal and immunofluorescence for VAMP4 (**Figure 1J**), another SNARE protein implicated in endosomal traffic (Martinez-Arca et al., 2001; Mallard et al., 2002; Tran et al., 2007). In spite of the many similarities between BLTP3A and BLTP3B, no fluorescence overlap was observed between BLTP3B-mRFP fluorescence and endogenous VAMP7 or VAMP4 immunoreactivity (**Supplemental Figure 1D**), revealing differences in the cargo of BLTP3A and BLTP3B vesicles. However, BLTP3A-mRFP accumulations also overlapped with the immunofluorescence of endogenous ATG9A, a component of autophagosome precursor vesicles, (**Figure 1J**), as previously observed for BLTP3B-mRFP (Hanna et al., 2022) (**Supplemental Figure 1D**).

The association of BLTP3A with lysosomes is mediated by its N-terminal region where the Rab7 binding site is located

To confirm that Rab7 is responsible for the association of BLTP3A-positive vesicles with lysosomes (Gillingham et al., 2019), BLTP3A-mRFP was co-expressed in RPE-1 cells with either WT RAB7 (GFP-Rab7$_{WT}$) or dominant negative (DN) Rab7 (GFP-Rab7$_{T22N}$), i.e. a mutant Rab7 that sequesters its guanylnucleotide exchange factor (GEF) to prevent formation of GTP-loaded Rab7 (**Figure 2A**) (Stenmark and Olkkonen, 2001). The coexpression of WT Rab7, which localized along the entire surface of endolysosomes, but not within the vesicle clusters, did not alter the localization of BLTP3A-mRFP (**Figure 2A**). In contrast, coexpression of GFP-Rab7$_{T22N}$ abolished the association of BLTP3A-mRFP foci with lysosomes and induced the expansion of the BLTP3A foci free in the cytoplasm (**Figure 2A**), which CLEM confirmed to represent large accumulations of vesicles no longer associated with lysosomes (**Figure 2B**).

In order to determine the region of BLTP3A responsible for the association with Rab7, which could provide insight into the orientation of BLTP3A at the lysosome-vesicle interface, we generated chimeras of BLTP3A and BLTP3B using BLTP3B tagged with mRFP at its C terminus as a backbone (**Figure 2C**). As BLTP3B does not associate with Rab7 in spite of its close similarity to BLTP3A, we searched for a.a. sequences of BLTP3A which would confer Rab7 binding and lysosome localization to BLTP3B. A chimera (BLTP3$_{chimera-1}$) in which its first RBG module (a.a. 1-125, which includes the so-called chorein domain) was replaced by the first RBG module of BLTP3A (a.a 1-125) formed large clusters but such clusters were not associated with lysosomes

(**Figure 2D**), as expected for BLTP3B. In contrast, a chimera ($BLTP3_{chimera-2}$) in which its second RBG module (a.a. 126-319) was replaced by the equivalent module of BLTP3A (a.a. 126-322) localized to LAMP1-GFP compartments similar to WT BLTP3A (**Figure 2D**), suggesting that the second RBG module of BLTP3A is sufficient for the Rab7-dependent lysosomal localization.

Moreover, a truncated construct comprising the first 2 RBG motifs of BLTP3A plus the first β-strand of the third RBG module of the same protein resulted in a fusion protein ($BLTP3A_{1-336}$-mRFP) that localized at lysosomes (**Figure 2D & 2E**), confirming the presence of the Rab7 binding site in this BLTP3A fragment. Notably, this fragment decorated homogenously the entire lysosomal surface, without forming the foci on their surface that reflect vesicle accumulations. These findings were further supported by the exogenous expression of Rab7 constructs. Expression of WT Rab7 greatly enhanced the localization of $BLTP3A_{1-336}$-mRFP around the entire lysosomal surface (**Figure 2F**), while the expression of dominant negative Rab7 (GFP-$Rab7_{T22N}$) resulted in a diffuse localization of $BLTP3A_{1-336}$-mRFP throughout the cytosol (**Figure 2F**). We conclude that a portion of BLTP3A near its N-terminus is necessary and sufficient for the localization of BLTP3A at lysosomes.

The C-terminal region of BLTP3A mediates its interaction with vesicles.

Rab7-dependent binding of BLTP3A to lysosomes via its N-terminal region implies that its C-terminal portion is likely responsible for vesicle binding and clustering (**Figure 2G**). To test this hypothesis, we generated BLTP3A constructs with C-terminal deletions and expressed them in cells also expressing dominant negative Rab7 (GFP-$Rab7_{T22N}$) to determine whether they could still cluster vesicles (**Figure 3A**). Deletion of the C-terminal helix of BLTP3A and of the linker that connects this helix to the last RBG motif ($BLTP3A_{1-1364}$-mRFP) did not affect the property of BLTP3A to cluster VAMP7-vesicles (detected by immunofluorescence using antibodies against VAMP7) similar to wild-type BLTP3A. However, a further truncation (construct $BLTP3A_{1-1327}$-mRFP) including the last two beta-strands of the sixth and final RBG motif of the channel, resulted in a protein that was diffusely cytosolic and did not cluster vesicles. The only accumulation of BLTP3A observed in these cells was a single cluster close to the nucleus (**Figure 3A**), most likely reflecting its interaction with Rab45 at the centrosomal area (**Supplemental Figure 1A**), but this cluster was VAMP7 negative, in agreement with the loss of vesicle binding (**Figure 3A**) Neither C-terminal truncation abolished localization to lysosomes (**Supplemental Figure 1E**). We conclude that the C-terminal portion of BLTP3A is necessary to interface with small vesicles.

We also attempted to identify BLTP3A binding partners on the vesicles. Towards this aim, we carried out anti-V5 affinity purification from non-ionic detergent solubilized A549 cells where BLTP3A was tagged at the endogenous locus, i.e. experimental conditions optimally suited to reveal physiological binding partners (**Figure 3B**). Affinity-purified proteins were then identified by mass spectrometry (**Figure 3C**). Unedited A549 cells were used as controls. This search did not identify any obvious candidate binding protein. While two of the top specific hits, Rab27B and its effector melanophilin (MLPH) are membrane associated proteins of transport vesicles (Nagata et al., 1990; Ménasché et al., 2000; Hume et al., 2001; Bahadoran et al., 2001; Nagashima et al., 2002; Strom et al., 2002), we failed to obtain evidence for a concentration of these proteins on

322 BLTP3A-positve vesicles. Thus these two proteins were not further studied in the context of the
323 present study. Two other top hits, however, the two mATG8 family members GABARAP and
324 MAP1LC3B, provided insight into properties of BLTP3A which will be discussed below.
325
326 **Lysosomal damage disrupts the Rab7-dependent association of BLTP3A positive vesicles**
327 **with lysosomes**
328
329 Perturbation of the membranes of lysosomes, for example by L-Leucyl-L-Leucine methyl ester
330 (LLOMe), a dipeptide taken-up into lysosomes where it is metabolized into membranolytic
331 peptides (Goldman and Kaplan, 1973; Thiele and Lipsky, 1990; Uchimoto et al., 1999), was
332 reported to trigger the rapid recruitment of factors to their surface that may help prevent or repair
333 damage (Skowyra et al., 2018; Radulovic et al., 2018; Shukla et al., 2022; Herbst et al., 2020;
334 Radulovic et al., 2022; Tan and Finkel, 2022; Bentley-DeSousa and Ferguson, 2023; Wang et al.,
335 2024a). These include, besides ESCRT components, shuttle-like lipid transfer proteins such as
336 ORP family members (Tan and Finkel, 2022; Radulovic et al., 2022) and bridge-like lipid transfer
337 proteins structurally related to BLTP3A (Wong et al., 2019; Neuman et al., 2022) such as VPS13C
338 (Wang et al., 2024a) and ATG2 (Tan and Finkel, 2022; Cross et al., 2023). Both VPS13C and
339 ATG2 are thought to mediate bulk phospholipid delivery to damaged lysosomes from the ER,
340 which they bind via their N-terminal chorein domain (Kumar et al., 2018; Valverde et al., 2019;
341 Osawa et al., 2019; Maeda et al., 2019; Wang et al., 2024a).
342
343 Although a pool of BLTP3A is already at contacts with lysosomes under control conditions (but in
344 an opposite orientation relative to that of the ATG2 and VPS13C at contacts of the ER with
345 damaged lysosomes, i.e. with its N-terminal chorein domain facing the lysosomal membrane), we
346 explored whether LLOMe dependent damage of lysosomes had an impact on BLTP3A
347 localization in RPE-1 cells. Surprisingly, and in contrast to the damage-dependent recruitment of
348 VPS13C (Wang et al., 2024a) and ATG2 (Tan and Finkel, 2022) to lysosomes, the focal
349 accumulations of BLTP3A on lysosomes, which reflect accumulations of BLTP3A-positive
350 vesicles, dissociated within minutes from the lysosomal surface upon its damage (**Figure 4A**),
351 whose occurrence was confirmed by the recruitment of cytosolic IST1 (mApple-IST1) (**Figure**
352 **4A**), an ESCRT-III subunit (Skowyra et al., 2018; Corkery et al., 2024). This LLOMe-dependent
353 dissociation of BLTP3A positive vesicle clusters from lysosomes, however, was not accompanied
354 by a dispersion of the vesicle clusters themselves, indicating that the Rab7-dependent interaction
355 of BLTP3A with lysosomes, not the interactions of BLTP3A which bind and clusters vesicles, was
356 perturbed. This was confirmed by the finding that the Rab7 binding N-terminal fragment of
357 BLTP3A ($BLTP3A_{1-336}$-mRFP), which does not bind vesicles, dissociated from lysosomes,
358 visualized in this experiment by the lysosomal protein NPC1 (NPC1-GFP) (**Figure 4B**).
359 Mechanisms responsible for the dissociation of BLTP3A from lysosomes remain unknown.
360 BLTP3A dissociation was not due to loss of Rab7 binding sites on lysosomes as the binding of
361 VPS13C, which is recruited to lysosomes with a kinetic similar to that of BLTP3A dissociation,
362 requires active Rab7 at these organelles (Wang et al., 2024a). Likewise dissociation was not due
363 to the rapid phosphorylation of Rab7 at serine 72, a process primarily mediated by the kinase
364 activity of LRRK1 (Wang et al., 2024a) with an additional variable contribution of the kinase TBK1
365 (Nirujogi et al., 2021; Fujita et al., 2022; Heo et al., 2018; Talaia et al., 2024), as over-expression

366 of a dominant-protein kinase active LRRK1 mutant (GFP-LRRK1^{K746G}) did not affect the
367 localization of BLTP3A-mRFP foci next to lysosomes in RPE-1 cells (**Supplemental Figure 1F &**
368 **Supplemental Figure 1G**).
369
370 **CASM activation induces the reassociation of BLTP3A with lysosomal membranes**
371
372 One event triggered by LLOMe-dependent damage of the lysosomal membrane is activation of
373 CASM (Conjugation of Atg8 to Single Membranes) (Durgan and Florey, 2022; Boyle et al., 2023;
374 Corkery et al., 2023; Kaur et al., 2023; Fischer et al., 2020). This is the process whereby lysosome
375 perturbations that drive V-ATPase V0-V1 association in their membrane to enhance its proton
376 pump activity also result in the recruitment of a subset of components of the classical autophagy
377 pathway resulting in the lipidation and recruitment to the lysosomal membrane of mATG8 family
378 proteins. These are small adaptors that are recruited to membranes in response to their triggered
379 conjugation to PE or PS and bind proteins which contain the so-called LC3-interacting region
380 (LIR) motif, typically found in disordered protein regions (Rogov et al., 2023). Atg8 family proteins,
381 which comprise six members in mammals, are well established players in conventional autophagy
382 (Melia et al., 2020; Nieto-Torres et al., 2021; Figueras-Novoa et al., 2024; Deretic et al., 2024):
383 they interact with the isolation membrane via their lipid tail and recruit cargo targeted for
384 autophagy via their LIR-motif-dependent interactions. However, the discovery of CASM has now
385 revealed another important role of these proteins which is being intensely investigated (Durgan
386 and Florey, 2022).
387
388 In view of the identification of two mATG8 proteins, MAP1LC3B and GABARAP, as interactors of
389 BLTP3A (**Figure 3C**), we further explored a potential role of CASM in BLTP3A dynamics. A search
390 for LIR motifs in BLTP3A using the publicly available iLR Autophagy Database
391 (https://ilir.warwick.ac.uk/index.php) predicts such a motif [Position Specific Scoring Matrix
392 (PSSM) score: 16] within a disordered loop projecting out from the C-terminal region of BLTP3A,
393 but not of BLTP3B, from several mammalian species, including humans (aa 1129-1134) (**Figure**
394 **5A**) (see also (Tu and Brumell, 2020)). The high degree of conservation of this motif relative to its
395 surrounding a.a. sequences suggests its physiological importance, consistent with our co-affinity
396 purification results. Moreover, structure-prediction algorithms (Abramson et al., 2024) predict with
397 high confidence an interaction between the LIR motif of BLTP3A and the majority of the six known
398 mATG8 proteins (**Supplemental Figure 2A & 2B**).
399
400 To determine a potential physiological role of an mATG8-BLTP3A interaction, we co-expressed
401 BLTP3A-mRFP and GFP-LC3B in RPE-1 cells. The localization of BLTP3A-mRFP on lysosomes
402 and to large accumulations was not changed by the over-expression of GFP-LC3B, which was
403 mostly cytosolic (**Figure 5B**). Starvation of these cells resulted in the formation of GFP-LC3B-
404 positive foci, as expected, but did not alter the localization of BLTP3A-mRFP, indicating that
405 BLTP3A does not play a role in conventional autophagy (**Figure 5B**).
406
407 We next monitored the response of LC3B relative to BLTP3A after addition of LLOMe. In the first
408 few minutes after LLOMe addition, when BLTP3A-mRFP clusters as described above dissociated
409 from lysosomes, GFP-LC3B fluorescence remained cytosolic with no overlap with the BLTP3A

410 fluorescence (**Figure 5C**). After ~5-10 mins of LLOMe treatment, however, GFP-LC3B began to
411 accumulate on the surface of some lysosomes (**Figure 5C**), as previously reported (Cross et al.,
412 2023), and this association correlated with the reassociation of a pool of BLTP3A-mRFP to such
413 lysosomes, consistent with BLTP3A being an mATG8 effector. This BLTP3A pool colocalized with
414 LC3 along the entire surface of lysosomes and did not occur in focal accumulations indicating that
415 it did not reflect presence of large vesicle clusters, although large BLTP3A positive larger clusters
416 persisted in the surrounding cytoplasm (**Figure 4A & Figure 5C**). Similar results were observed
417 upon addition of the lysosome stressor glycyl-L-phenylalanine 2-naphthylamide (GPN)
418 (**Supplemental Figure 2C**) (Chen et al., 2024; Durgan and Florey, 2022), another CASM
419 activator. Deletion of the LIR motif of BLTP3A (BLTP3AΔLIR-mRFP) did not affect the localization
420 of BLTP3A in the absence of LLOMe treatment and did not abolish the shedding of BLTP3A
421 clusters upon LLOMe treatment but abolished its recruitment to GFP-LC3B positive lysosomes
422 after LLOMe (**Figure 5D**), demonstrating that the LIR motif of BLTP3A is necessary for such
423 recruitment.
424
425 The absence of large vesicle clusters around LC3-positive lysosomes was further corroborated
426 by correlative fluorescence-focused ion beam scanning electron microscopy (FIB-SEM), which
427 allowed us to obtain views of the entire surface of lysosomes in RPE-1 cells positive for
428 exogenous BLTP3A-mRFP and GFP-LC3B after 15 mins of LLOMe exposure (**Figure 5E**). Only
429 scattered vesicles were observed on such lysosomes (**Figure 5E**), in strong contrast with the
430 massive accumulation of vesicles observed in the absence of LLOMe (**Figure 1H**). Importantly,
431 correlative fluorescence-FIB-SEM microscopy also showed abundant presence of ER contacts
432 (**Figure 5E, Supplemental Movie 1 & 2**), as expected after LLOMe treatment (Tan and Finkel,
433 2022; Radulovic et al., 2022; Wang et al., 2024a).
434
435 **Recruitment of BLTP3A to vacuoles containing internalized crystals corroborates its**
436 **identification as a CASM effector**
437
438 To validate our model that BLTP3A is an effector of CASM, we used a manipulation alternative to
439 LLOMe to activate this pathway. Monosodium urate (MSU) crystals, which are readily taken up
440 by phagocytosis and accumulate within intracellular vacuoles, are known activators of CASM
441 (Cross et al., 2023). MSU crystals added to RPE-1 cells for 2 hrs were easily observed by
442 brightfield microscopy (**Figure 6A**). After internalization they accumulated in LAMP1-positive
443 vacuoles, many of which were decorated by LC3, consistent with these crystals being CASM
444 activators (Cross et al., 2023). In cells expressing BLTP3A-mRFP along with LAMP1-GFP or
445 GFP-LC3, a strong colocalization of BLTP3A-mRFP, but not of BLTP3A lacking the LIR motif
446 (BLTP3AΔLIR-mRFP) was observed with these proteins on crystal containing vacuoles (**Figure**
447 **6B & 6C**). We also used time-lapse fluorescence microscopy to capture the moments of CASM
448 activation (i.e. the accumulation of GFP-LC3B along the surface of a crystal-containing vacuole)
449 and observed a very close temporal correlation of GFP-LC3B and BLTP3A-mRFP recruitment
450 (**Figure 6D**), in agreement with BLTP3A being an effector of CASM.
451
452 **Loss of BLTP3A in A549 cells impacts lysosome homeostasis**
453

454 In view of the finding that BLTP3A is a factor responding to lysosome perturbation, we explored
455 the possibility that BLTP3A may have an impact on lysosome properties and/or in counteracting
456 lysosome damage. To this aim we generated BLTP3A KO cells. The BLTP3A gene was edited in
457 A549 cells to include frameshift mutations in exon 2 (**Supplemental Figure 2D**) and absence of
458 the BLTP3A protein in lysates from these cells was confirmed by western blotting (**Figure 7A**).
459 Interestingly, while levels of some proteins of the late endosomal system, for example Rab7, were
460 unchanged in the lysates of KO cells relative to controls, a ~5-fold decrease in the protein levels
461 of LAMP1 was observed (**Figure 7A & Supplemental Figure 2E)**, confirmed by a decrease of
462 anti-LAMP1 immunofluorescence, despite no obvious difference in lysosome number (**Figure**
463 **7B**), pointing to an important role of BLTP3A in lysosome homeostasis.
464
465 In order to assess the impact of the lack of BLTP3A on lysosome damage, we used the galectin-
466 3 (Gal3)-based immunofluorescence assay (**Figure 7C**). Gal3, which is normally diffuse in the
467 cytosol, binds to β-galactosides and accumulates within lysosomes only when the membrane of
468 these organelles is damaged. This accumulation results in bright puncta of anti-Gal3
469 immunofluorescence which corresponds to lysed lysosomes. Upon addition of LLOMe to A549
470 cells, bright puncta of Gal3 immunoreactivity started to appear in both wild-type and BLTP3A KO
471 cells, (**Figure 7C**). However, at the 30 and 60 min timepoints, a higher number of Gal3 spots were
472 observed in BLTP3A KO cells relative to wild-type cells (**Figure 7D**) revealing a greater fragility
473 of KO cells. These findings suggest that the recruitment of BLTP3A to lysosomes may play a role
474 in the resilience and/or response of these organelles to damage.
475
476 **DISCUSSION**
477
478 Our study shows that BLTP3A, a protein expected to transfer lipids between adjacent membranes
479 via a bridge-like mechanism, is a component of protein networks implicated in membrane traffic
480 in late endosomes/lysosomes and that lysosome damage has an impact on its localization.
481 BLTP3A binds and cluster vesicles of the endocytic system positive for VAMP7 and VAMP4 and
482 tether them to lysosomes via an interaction of its N-terminal region with lysosome-bound Rab7.
483 Upon lysosome membrane damage and the subsequent recruitment to their surface of mATG8
484 family proteins via CASM, this Rab7-dependent interaction is disrupted. However, within minutes,
485 BLTP3A then reassociates with lysosomes by interacting with mATG8 proteins via a LIR motif
486 present in a long predicted unfolded loop emerging form the C-terminal region of the protein. As
487 we discuss below, we suggest that BLTP3A may cooperate with other BLTPs in the response of
488 cells to lysosome damage. Accordingly, we have found evidence for an increased fragility of
489 lysosomes in response to damage in BLTP3A KO cells.
490
491 The property of BLTP3A to associate with small vesicles and induce their striking accumulation
492 when overexpressed is shared with BLTP3B (Hanna et al., 2022). Moreover, BLTP3A- and
493 BLTP3B-positive vesicles have similar size, share at least one cargo, ATG9A, and clusters of
494 them are closely associated to other organelles. However, these organelles differ for the two
495 proteins: Rab5 positive early endosomes in the case of BLTP3B and Rab7 positive lysosomes in
496 the case of BLTP3A. Moreover, BLTP3A and BLTP3B positive vesicles differ at least partially in

497 protein composition, as only BLTP3A positive clusters are strongly immunolabeled by antibodies
498 directed against VAMP7 and VAMP4.
499
500 BLTP3 vesicle clusters are reminiscent of the clusters of synaptic vesicles at synapses. Such
501 clusters were shown to have the properties of liquid biomolecular condensates (Milovanovic and
502 De Camilli, 2017; Milovanovic et al., 2018; Park et al., 2021). Similarly, vesicle clusters involving
503 BLTP3A and BLTP3B are very dynamic (see for example movies of these clusters in (Hanna et
504 al., 2022)). The assembly of BLTP3A-positive vesicle clusters and their anchorage to
505 endosomes/lysosomes, implies a minimum of three direct or indirect interactions of BLTP3A: 1)
506 an interaction with vesicles, 2) an interaction with itself or with adaptor proteins to cluster vesicles
507 and 3) an interaction with lysosomes to account for the anchoring of the vesicle clusters to these
508 organelles.
509
510 We have shown that the interaction with lysosomes of vesicle-associated BLTP3A (interaction
511 #3) is mediated by the binding to lysosome-bound Rab7, consistent with its being a Rab7 effector.
512 Moreover, our results suggest that such an interaction involves the N-terminal region of BLTP3A,
513 where we have detected the Rab7 binding site. We have also shown that the binding to vesicles
514 (interaction #1) is mediated by the opposite end of the protein, i.e. its C-terminal region, but so
515 far, we have not detected a binding partner. We note that even in the case of synaptic vesicle
516 condensates (Milovanovic et al., 2018; Park et al., 2021), which involve interactions between
517 synapsin (a cytosolic protein) (Südhof et al., 1989; De Camilli et al., 1990), and synaptophysin (a
518 vesicle protein) (Johnston et al., 1989), a direct interaction between the two proteins could not be
519 detected by co-precipitation (Park et al., 2021), although clearly such an interaction occurs in
520 living cells where low affinity is counteracted by multivalency: a multiplicity of low affinity
521 interactions between synapsin with itself and with synaptophysin, a protein present in multiple
522 copies on the vesicles.
523
524 Concerning the mechanisms responsible for vesicle clustering (interaction #2), these may involve
525 self-association of BLTP3A via low complexity unfolded sequences that project out of its rod-like
526 core, or binding of BLTP3A to yet to be discovered adaptor/crosslinker proteins. As the property
527 to cluster vesicles is shared by both BLTP3A and BLTP3B, such a property must rely on shared
528 molecular determinants of these two proteins. Ongoing work is addressing these mechanisms.
529 The property of BLTP3 proteins to cluster vesicles into small packages may be an important
530 aspect of their physiological function as BLTP3B-positive vesicles were shown to be organized in
531 small clusters even at physiological levels of expression (Hanna et al., 2022). Large clusters likely
532 result from BLTP3 overexpression, although other scenarios, such as that BLTP3 overexpression
533 may result in vesicle accumulation due to a dominant negative effect on their fusion with
534 downstream targets, cannot be ruled out.
535
536 Our study indicates that the Rab7-dependent association of BLTP3A with lysosomes requires a
537 portion of BLTP3A located in proximity of its N-terminal region, the so-called chorein motif (Kumar
538 et al., 2018). In most other BLTP family members, the chorein or chorein-like motifs are localized
539 at the ER, which is typically thought to be the “donor” membrane in their lipid transfer function
540 (Kumar et al., 2018; Valverde et al., 2019; Guillén-Samander et al., 2021; Cai et al., 2022b;

Levine, 2019; Osawa et al., 2019). This is also the case for the other two BLTPs reported to be implicated in ER to lysosomes lipid flux, VPS13C (Kumar et al., 2018; Wang et al., 2024a) and ATG2 (Tan and Finkel, 2022; Cross et al., 2023). Thus, we consider it unlikely that the orientation of BLTP3A when cross-linking vesicles to Rab7 may be relevant to its lipid transfer properties.

Lysosomal membrane damage activates multiple response mechanisms at timepoints ranging from seconds to hours (Skowyra et al., 2018; Radulovic et al., 2018; Tan and Finkel, 2022; Meyer and Kravic, 2024; Wang et al., 2024a). Conjugation of mATG8 proteins to the surface of lysosomes (CASM pathway) is one such response (Durgan and Florey, 2022). mATG8 proteins can be detected on lysosomes ~5-10 mins after the initiation of membrane damage, similar to the time frame of BLTP3A reassociation. It is therefore of great interest that 1) top hits identified from our immunoprecipitation of endogenously tagged BLTP3A^V5 from A549 cells are two mATG8 proteins (MAP1LC3B and GABARAP) and 2) BLTP3A contains a LIR motif (i.e. an Atg8 binding consensus) within a disordered loop projecting out of the C-terminal rod-like region. Accordingly, we found that the reassociation of BLTP3A after LLOMe follows the accumulation of LC3B on the surface of lysosomes and that the LIR motif is required for the reassociation of BLTP3A with their surface.

The LIR motif of BLTP3A is localized on a long (305 a.a.) predicted unfolded loop emerging from the C-terminal portion of BLTP3A, which is the portion of the protein expected to bind vesicles. However, although clusters of BLTP3A positive vesicles persist in the cytoplasm, the bulk of the pool of BLTP3A that reassociates with the lysosomal surface is not bound to small vesicles, suggesting that the LIR motif-dependent interaction of BLTP3A with lysosome-bound LC3B is mutually exclusive with its association with vesicles. A binding of BLTP3A to lysosomes via its LIR motif, rather than by Rab7, would leave its N-terminal chorein domain region, no longer engaged by Rab7, available for an interaction with the ER, a possibility that needs to be further explored.

Lysosome membrane damage is known to result in the formation of ER-lysosome tethers comprising other lipid transfer proteins, such as ORP proteins (Tan and Finkel, 2022; Radulovic et al., 2022), VPS13C (Wang et al., 2024a) and ATG2 (Tan and Finkel, 2022; Cross et al., 2023), most likely as a cellular response aimed at protecting or repairing membranes by delivering new lipids. We suggest that under these conditions BLTP3A may be available on the surface of damaged lysosomes to function at close appositions between lysosomes and the ER where it may cooperate with other BLTPs in transferring membrane lipids to lysosomes. However, we note an important limitation of this study: although the structure and biochemical properties of BLTP3A suggest that it may transfer lipids between two membranes via a bridge-like mechanism, the precise mechanism(s) through which this putative function plays a role in lysosome biology and in response to lysosome damage remains unclear and is the primary focus of our future studies. As lysosomes play a key role in cells of the immune system, it is of special interest that several coding variants of BLTP3A are associated with susceptibility to systemic lupus erythematosus (SLE) (Gateva et al., 2009; Zhang et al., 2011; Wen et al., 2020), a chronic autoimmune disease.

MATERIALS AND METHODS

585
586 **Antibodies and Reagents**
587
588 The list of plasmids, antibodies, their working dilution, and the supplier for this study can be
589 found in the **Key Resource Table** at the following link:
590 https://docs.google.com/spreadsheets/d/1RVOPrz9L_QFf1PetDbkS3vPMHXVXI_QYCKIUzjgA3
591 lc/edit?usp=sharing
592
593 **Generation of Plasmids**
594
595 All BLTP3A and BLTP3B ORFs used in this study utilized a human codon optimized sequence
596 designed and purchased from Genscript. Codon optimized human BLTP3 chimeras were
597 amplified using PCR from the pcDNA3.1 plasmid and ligated into a pmCh-N1 plasmid. Most
598 constructs were generated with regular cloning protocols or through site-directed mutagenesis.
599 The desired ORFs were amplified by PCR and inserted into plasmids through enzyme digestions
600 and ligation. Some amplified ORFs were ligated using HiFi assembly (NEB). Details of primer
601 sets, enzymes, techniques, and plasmids used for each construct can be found in the **Key**
602 **Resource Table**.
603
604 Detailed protocol for the molecular cloning of BLTP3 plasmids for expression in mammalian cells
605 is at: https://dx.doi.org/10.17504/protocols.io.8epv5z5kjv1b/v1
606
607 **Correlative Light and Electron Microscopy**
608
609 For TEM CLEM, RPE-1 cells were plated on 35 mm gridded, glass-bottom MatTek dish (P35G-
610 1.5-14-CGRD) and transfected as described above with BLTP3A-mRFP, LAMP1-GFP, mito-BFP.
611 Cells were pre-fixed in 4% PFA in dPBS then washed with dPBS before fluorescence light
612 microscopy imaging. Regions of interest were selected and their coordinates on the dish were
613 identified using phase contrast. Cells were further fixed with 2.5% glutaraldehyde in 0.1 M sodium
614 cacodylate buffer, postfixed in 2% OsO_4 and 1.5% $K_4Fe(CN)_6$ (Sigma-Aldrich) in 0.1 M sodium
615 cacodylate buffer, *en bloc* stained with 2% aqueous uranyl acetate, dehydrated in graded series
616 of ethanols (50%, 75%, and 100%), and embedded in Embed 812. Cells of interest were relocated
617 based on the pre-recorded coordinates. Ultrathin sections (50-60 nm) were post-stained with
618 uranyl acetate substitute (UranyLess, EMS), followed by a lead citrate solution. Sections were
619 observed in a Talos L 120C TEM microscope at 80 kV, images were taken with Velox software
620 and a 4k × 4K Ceta CMOS Camera (Thermo Fisher Scientific). Except noted all reagents were
621 from EMS (Electron Microscopy Sciences), Hatfield, PA.
622
623 Detailed protocol for 2D TEM CLEM is at:
624 https://dx.doi.org/10.17504/protocols.io.261gend2jg47/v1
625
626 **FIB-SEM Sample Preparation and Imaging**
627

One Epon-embedded sample of RPE-1 cells expressing BLTP3A-mRFP and GFP-LC3B after 15 mins of LLOMe exposure, was mounted onto the top of a 1 mm copper stud using Durcupan, ensuring optimal charge dissipation by maintaining contact between the heavy metal-stained sample and the copper stud. The vertical sample post was then trimmed to a small block containing the Region of Interest (ROI), with dimensions of 80 µm in width (perpendicular to the ion beam) and 75 µm in depth (in the ion beam direction). Precise ROI targeting and trimming were achieved using overlay images from light fluorescence microscopy and X-ray tomography data acquired with a Zeiss Versa XRM-620. The detail approach was previously described by (Pang and Xu, 2023). To enhance conductivity, thin layers of conductive material—10 nm of gold followed by 40 nm of carbon—were deposited onto the trimmed sample using a Leica EM ACE600 coater.

The FIB-SEM prepared sample was imaged using a customized enhanced FIB-SEM microscope (Xu et al., 2017, 2021). The images were acquired using a 500 pA current SEM probe at 0.7 keV. The scan rate was 400 kHz, with a 2-nm pixel along x and y axes. A 2-nm z-step was achieved by ~5 seconds of milling with a 15-nA Ga^+ beam at 30 kV. A total volume of 12 × 6 × 12 μm^3 was acquired over 8 days at a rate of 1 minute per frame. The raw image stack was aligned using a SIFT based MATLAB script and binned 2-to-1 along x, y, and z axes to create a final dataset with 4 × 4 × 4 nm^3 voxels, which can be viewed in any arbitrary orientations.

Cell culture and Transfections

hTERT-RPE-1 cells were a kind gift of A. Audhya (University of Wisconsin, Madison, WI). A549 and COS-7 cells were obtained from ATCC. All mammalian cells were maintained at 37ºC in humidified atmosphere at 5% CO_2 unless noted otherwise. A549 and COS-7 cells were grown in DMEM and RPE-1 cells in DMEM/F12 medium (Thermo Fisher Scientific) supplemented with 10% FBS, 100 U/mL penicillin, 100mg/mL streptomycin. 2mM glutamax (Thermo Fisher Scientific) was added to all media for RPE-1 cells. All cell lines were routinely tested and always resulted free from mycoplasma contamination.

Transient transfections were carried out on cells that were seeded at last 8 h prior. All transfections of plasmids used FuGENEHD (Promega) to manufacturers specifications for 16-24 h in complete media without antibiotics.

Detailed protocol for cell culture, transfection, immunocytochemistry, and imaging: https://dx.doi.org/10.17504/protocols.io.eq2lyp55mlx9/v1

Immunoblotting and Imaging Procedure

All cell samples analyzed by immunoblotting were scraped from plates and harvested by centrifugation (500xg for 5 minutes). The pellet was washed with ice-cold dPBS and centrifuged again in a 1.7mL Eppendorf tube. The cell pellet was resuspended in Lysis buffer (20mM Tris-HCl pH 7.5, 150mM NaCl, 1% SDS, 1mM EDTA) containing protease inhibitor cocktail (Roche). The lysate was clarified by centrifugation (17,000xg for 10 minutes) and a small portion of lysate

672 was reserved for quantification of protein concentration by Bradford. The remaining lysate was
673 then mixed with 5x SDS sample buffer (Cold Spring Harbor) to 1x concentration and then heated
674 to 95°C for 3 minutes. 15-25ug of protein samples were separated by electrophoresis on a 4-20%
675 Mini-PROTEAN TGX gel and then subjected to standard western blot transfer and procedures.
676 Blots were imaged using the Odyssey imaging system (LI-COR) using manufacturers protocols.
677 All primary antibodies used in this study are listed in the **Key Resource Table**.
678
679 **Mouse Tissue Lysate Preparation**
680
681 Tissues were collected from sacrificed WT C57BL/6J mice (Jackson Laboratory strain #000664).
682 For each 1 g of material, 10 ml of buffer (25 mM Hepes, pH 7.4, 200 mM NaCl, 5% glycerol,
683 protease inhibitors) was added. Mechanical lysis was performed using a glass dounce-
684 homogenizer (15 strokes). Triton X-100 was added to 1%, and material was rotated at 4°C for 30
685 min. Material was centrifuged at 1,000 g to remove cell debris and the collected supernatant was
686 centrifuged at 27,000 g for 20 min. The resulting supernatant mixed was flash frozen and stored
687 at −80°C until use.
688
689 **Live Cell Imaging and Immunofluorescence**
690
691 For all live cell microscopy cells were seeded on glass-bottom mat-tek dishes (MATtek
692 corporation) 5500/cm^2 in complete media. Transfections were carried out as described above.
693 Spinning-disk confocal imaging was preformed 16-24 h post transfection using an Andor
694 Dragonfly 200 (Oxford Instruments) inverted microscope equipped with a Zyla cMOS 5.5 camera
695 and controlled by Fusion (Oxford Instruments) software. Laser lines used: DAPI, 440nm; GFP,
696 488; RFP, 561; Cy5, 647. Images were acquired with a PlanApo objective (60x 1.45-NA). During
697 imaging, cells were maintained in Live Cell Imaging buffer (Life Technologies) in a cage incubator
698 (Okolab) with humidified atmosphere at 37°C. LLOMe (Sigma-Aldrich, CAS: 1668914-8) and GPN
699 (Cayman Chemical, CAS: 14634) were dissolved in ethanol and used at a final concentration of
700 1 mM for all imaging experiments. All live imaging experiments are representative of at least 10
701 independent repeats.
702
703 Immunofluorescent experiments were performed with cells grown on #1.5 glass cover slips. Cells
704 were fixed with 4% PFA in PBS (Gibco, 14190144) for 15 mins at room temperature, washed 3x
705 with PBS, permeabilized using antibody dilution buffer (1x PBS containing 0.2% saponin and 2%
706 BSA) at 4°C overnight with the indicated primary antibodies. Slides were washed three times with
707 PBS containing 0.02% saponin to remove excess primary antibody and subsequently incubated
708 with secondary antibodies diluted in antibody dilution buffer for 45 min at room temperature in the
709 dark. Slides were washed again three times to remove secondary antibody with PBS containing
710 0.02% saponin prior to mounting.
711
712 **Lysosomotropic drug treatments**
713
714 Cells (RPE-1 or A549) were seeded 16-24 hrs before treatments. A fresh 333mM stock solution
715 of LLOMe in ethanol was prepared and kept on ice. For live-imaging experiments, a 2x stock of

716 LLOMe or GPN (2 mM) was prepared in complete media immediately before adding to an equal
717 volume of complete media on a Mattek dish. Cells were imaging at 37C with 5% CO2 at all times.
718 For lysosome damage experiments (galectin-3 immunofluorescence), LLOMe (1 mM) was added
719 to complete medium pre-warmed to 37C and immediately added to cells. Cells were then
720 incubated at 37C with 5% CO2 for 15, 30, or 60 minutes. Untreated cells received an identical
721 volume of vehicle (ethanol) in complete medium for 15 minutes and served as a baseline. After
722 incubation with LLOMe or vehicle, cells were fixed as described above before being incubated
723 overnight at 4C with antibodies against galectin-3.
724
725 **Quantification of Gal3 puncta in A549 cells**
726
727 Cell boundaries were drawn by hand in Fiji. Minimum and maximum display values of 3000 and
728 8000 were used to detect fluorescence. Remaining background signal after setting these
729 minimum and maximum display values was smoothened using the "Mean" filter in Fiji set to a
730 radius of 2 pixels. After smoothening, Fiji's default thresholding algorithm was used to identify the
731 foreground objects and create a mask of Gal3 spots. The resulting mask was processed using
732 Fiji's binary "Watershed" separation technique to separate foreground objects (Gal3 spots) that
733 were touching. Finally, using Fiji's "Analyze particles" function, ROIs were generated for all mask
734 objects and counted as individual Gal3 spots. ROIs smaller than 3 pixels were considered noise
735 and were not included in the count.
736
737 **Generation of CRISPR Edited Cell Lines**
738
739 Endogenous tagging of A549 cells was carried out using a CRISPR/Cas9 ribonucleoprotein
740 (RNP) complex. Commercially purified Cas9 nuclease (IDT) was combined and incubated with
741 trans-activating CRISPR RNA (tracrRNA) and a BLTP3A-targeting guide RNA to form the RNP
742 complex. The RNP complex was then incubated with a single-stranded repair template containing
743 the insert sequence and ultimately delivered to A549 cells via electroporation. Subsequently, the
744 RNP-transfected pools were serially diluted and plated at 1 cell per well on a glass bottom 96-
745 well plate. Wells were expanded and tested for editing via PCR until an appropriate number of
746 edited clones were obtained. All gRNAs used in this study are listed in the **Key Resource Table**.
747
748 **Immunoprecipitation of Endogenously Tagged BLTP3A**
749
750 Wild-type or endogenously edited A549 cells expressing BLTP3A^V5 were grown to 90%
751 confluency on 15 cm plates (Falcon). Two 15 cm plates were used for each independent replicate
752 of wild-type and edited cells (n=3). Cells were washed with dPBS (Gibco) and then scrapped from
753 the surface of the plates into 2 mL of dPBS per plate. Cells were pelleted at 1000g for 5 min and
754 the dPBS supernatant was removed. Cells were resuspended in 2 mL of ice-cold lysis buffer (50
755 mM Tris pH 7.6, 150 mM NaCl, 1% Triton X-100, protease inhibitors [Roche]) and rotated at 4°C
756 for 20 mins. Cell lysates were spun at 17000g for 10 mins to clear insoluble material. The
757 supernatants were then added to 75 uL (slurry) of anti-V5 magnetic resin (ChromoTek) and let
758 rotate at 4°C for 2 hrs. Resin was washed twice for 5 mins rotating with ice cold lysis buffer and

759 then washed a third time without detergent for 5 mins (50 mM Tris pH 7.6, 150 mM NaCl, protease
760 inhibitors). Supernatant was removed and resin was stored at −80°C.
761
762 **Protein digestion**
763
764 The beads were resuspended in 80 µL of 2M Urea, 50 mM ammonium bicarbonate (ABC) and
765 treated with DL-dithiothreitol (DTT) (final concentration 1 mM) for 30 minutes at 37°C with shaking
766 at 1100 rpm on a Thermomixer (Thermo Fisher). Free cysteine residues were alkylated with 2-
767 iodoacetamide (IAA) (final concentration 3.67 mM) for 45 minutes at 25°C with shaking at 1100
768 rpm in the dark. The reaction was quenched using DTT (final concentration 3.67 mM), and LysC
769 (750 ng) was added, followed by incubation for 1h at 37°C at 1150 rpm. Finally, trypsin (750 ng)
770 was added, and the mixture was incubated for 16 hours at 37°C with shaking at 1150 rpm.
771
772 After incubation, an additional 500 ng of trypsin was added to the sample, followed by a 2-hour
773 incubation at 37°C at 1150 rpm. The digest was then acidified to pH <3 by adding 50%
774 trifluoroacetic acid (TFA), and the peptides were desalted on C18 stage tips (Empore C18
775 extraction disks). Briefly, the stage tips were conditioned with sequential additions of: i) 100 µL
776 methanol), ii) 100 µL 70% acetonitrile (ACN)/0.1% TFA, iii) 100 mL 0.1% TFA twice. After
777 conditioning, the acidified peptide digest was loaded onto the stage tip, and the stationary phase
778 was washed with 100 µL 0.1% formic acid (FA) twice. Finally, the peptides were eluted with 50
779 µL 70% ACN/0.1% FA twice. Eluted peptides were dried under vacuum in a Speed-Vac
780 centrifuge, reconstituted in 12 µL of 0.1% FA, sonicated and transferred to an autosampler vial.
781 Peptide yield was quantified using a NanoDrop (Thermo Fisher).
782
783 **Mass spectrometry analyses**
784
785 Peptides were separated on a 25 cm column with a 75 µm diameter and 1.7 µm particle size,
786 composed of C18 stationary phase (IonOpticks Aurora 3 1801220) using a gradient from 2% to
787 35% Buffer B over 90 minutes, followed by an increase to 95% Buffer B for 7 minutes (Buffer A:
788 0.1% FA in HPLC-grade water; Buffer B: 99.9% ACN, 0.1% FA) with a flow rate of 300 nL/min on
789 a NanoElute2 system (Bruker).
790
791 MS data were acquired on a TimsTOF HT (Bruker) with a Captive Spray source (Bruker) using a
792 data-independent acquisition PASEF method (dia-PASEF). The mass range was set from 100 to
793 1700 *m/z*, and the ion mobility range from 0.60 V.s/cm^2 (collision energy 20 eV) to 1.6 V.s/cm^2
794 (collision energy 59 eV), a ramp time of 100 ms, and an accumulation time of 100 ms. The dia-
795 PASEF settings included a mass range of 400.0 to 1201.0 Da, mobility range 0.60-1.60, and an
796 estimated cycle time of 1.80 seconds. The dia-PASEF windows were set with a mass width of
797 26.00 Da, mass overlap 1.00 Da, and 32 mass steps per cycle.
798
799 **DIA data analysis**
800
801 Raw data files were processed using Spectronaut version 17.4 (Biognosys) and searched with
802 the PULSAR search engine against the Homo sapiens UniProt protein database (226,953 entries,

downloaded on 2022/09/23). Cysteine carbamidomethylation was set as fixed modifications, while methionine oxidation, acetylation of the protein N-terminus, and deamidation (NQ) were defined as variable modifications. A maximum of two trypsin missed cleavages was allowed. Searches used a reversed sequence decoy strategy to control the peptide false discovery rate (FDR), with a 1% FDR threshold for identification. An unpaired t-test was used to calculate p-values for differential analysis, and volcano plots were generated based on log2 fold change and q-value (multiple testing corrected p-value). A q-value of ≤0.05 was considered the statistically significant cut-off.

The mass spectrometry proteomics data have been deposited to the ProteomeXchange Consortium via the PRIDE partner repository with the dataset identifier PXD056338.

Image processing, Analysis, and Statistics

Florescence images presented in this study are representative of cells imaged in at least three independent experiments and were processed with ImageJ software. The dimensions of some of the magnification insets or panels were enlarged using the *Scale* function on ImageJ.

Statistical analysis was performed with GraphPad Prism 10 software. Groups were compared using a two-tail unpaired Student *t* test and results were deemed significant when a p value was smaller than 0.05.

ACKNOWLEDGMENTS

We thank Thomas Melia and Shawn Ferguson (Yale) for discussion and advice, James Liu (Janelia Res Labs) for advice on endogenous tagging, Dario Alessi (Dundee, UK) for the personal communication of unpublished data and Chase Amos, Hanieh Falahati, and Berak Ugur (De Camilli lab) for critical reading of the manuscript. We also thank the support provided by the FIB-SEM Collaboration Core at Yale School of Medicine.

FUNDING

National Institutes of Health grant DA018343 (PDC)
National Institutes of Health grant NS36251 (PDC)
Aligning Science Across Parkinson's ASAP-000580 (PDC)
National Institutes of Health P30 CA008748 (MM)

AUTHOR CONTRIBUTIONS

Conceptualization: MGH, PDC
Methodology: MGH, PDC, HRC, ZI, MM, YW, CSX, SP
Investigation: MGH, HRC, ZI, MM, YW, CSX, SP
Figures: MGH, YW, HRC
Supervision: PDC, MM

Writing—original draft: MGH, PDC
Writing—review & editing: MGH, PDC, HRC, MM, CSX, SP

Competing Interests

PDC is a member of the Scientific Advisory Board of Casma Therapeutics. No conflict exists with this role.

FIGURE LEGENDS

Figure 1: Endogenous and exogenous BLTP3A form accumulations that associate with lysosomes.

(A) AlphaFold prediction of full-length BLTP3A with ConSurf conservation scores (top left) for each a.a. or cross-section of surface rendering of BLTP3A channel (top right) highlighting hydrophobic residues (orange). Linear representation of BLTP3A: per residue ConSurf scores (top) and RBG organization (bottom). IDR, predicted intrinsically disordered region (light gray); CH, C-terminal helix (dark gray).
(B) Alignment of the a.a. of motifs important for the indicated protein interactions of BLTP3B with corresponding sequences of BLTP3A. ConSurf conservation scores for each a.a. is indicated by color (same color scheme as in Fig.1A)
(C) Western blot of lysates of wild-type mouse tissues for BLTP3A, BLTP3B, and vinculin as a loading control.
(D) Western blot of control and edited (BLTP3A^V5) cell clones for BLTP3A, V5, and alpha-tubulin as a loading control.
(E) Fluorescence images of endogenously edited (left) or parental control (middle) A549 cells with antibodies against LAMP1 (green) and V5 (magenta). Scale bar, 10 µm. The insets are a zoom of a small region of the cell. Scale bar, 1 µm. Right: Fluorescence of exogenous BLTP3A-GFP (green) in endogenously edited A549 cell. Scale bar, 5 µm. Insets: zoom of square region of cell showing co-localization of endogenous BLTP3A^V5 signal from immunolabeling with antibodies against V5 (magenta) and BLTP3A-GFP fluorescence (green). Scale bar, 1 µm.
(F) Fluorescence image of wild-type RPE-1 cell immunostained with antibodies against LAMP1 (green) and DAPI (blue). Scale bar, 5 µm.
(G) Fluorescence image of an RPE-1 cell expressing exogenous BLTP3A-mRFP (large field, inverted grays) and LAMP1-GFP (not shown). Scale bar, 5 µm. The area enclosed by a dotted rectangle is shown at right at high magnification with BLTP3A-mRFP in magenta and LAMP1-GFP in green (individual channels are shown as inverted grays). Red arrows indicate large BLTP3A accumulations not associated with lysosomes. Scale bar, 1 µm.
(H) CLEM of a BLTP3A-mRFP positive cluster in an RPE-1 cell. Left: florescence images of BLTP3A-mRFP (magenta). Scale bar, 1 µm. Right: EM micrograph of the field shown at left revealing that the BLTP3A-mRFP fluorescence reflects clusters of small vesicles, many of them tethered to the surface of lysosomes. Scale bar, 500 nm.
(I) Distance between the membranes of lysosomes and tethered vesicles from EM micrographs. Mean = 10.8 nm; standard error of the mean = ±0.20 nm.

892 **(J)** Left: Fluorescence image of an RPE-1 cell expressing exogenous BLTP3A-mRFP (inverted
893 grays) and immunolabeled with antibodies against VAMP7 (shown in the high mag fields at right).
894 Scale bar, 5 µm. Right: zooms of different RPE-1 cells expressing exogenous BLTP3A-mRFP
895 (magenta) and immunolabeled (green) with antibodies against the following endogenous proteins,
896 VAMP4 and ATG9A. Individual channels are shown as inverted grays. Merge of channels on
897 bottom. Scale bar, 1 µm.
898
899 **Figure 2: The N-terminus of BLTP3A associates with Rab7 on the surface of lysosomes.**
900
901 **(A)** Fluorescence images of RPE-1 cells expressing exogenous BLTP3A-mRFP (shown in
902 inverted grays) and (not shown) GFP-tagged wild type Rab7 (left) or dominant negative (DN)
903 Rab7 (T22N) (right). Scale bar, 5 µm.
904 **(B)** CLEM of a BLTP3A-mRFP positive cluster in an RPE-1 cell expressing GFP-tagged dominant
905 negative Rab7. Left: fluorescence image (magenta). Scale bar, 1 µm. Right: EM micrograph of
906 the field shown at left revealing that the BLTP3A-mRFP fluorescence reflects clusters of small
907 vesicles. Scale bar, 500 nm.
908 **(C)** BLTP3 chimeras design. Left: Surface representation of the predicted RBG core of BLTP3A.
909 Red and blue indicate positive and negative charges, respectively, and gray indicates
910 hydrophobic surfaces. Right: Surface representation (top) and ribbon representation (bottom) of
911 the "untwisted" protein showing individual RBG motifs. Bottom: Cartoon of chimeras consisting of
912 BLTP3A (dark orange) and BLTP3B (light orange) RBG motifs.
913 **(D)** High-magnification live fluorescence images of RPE-1 cells expressing the indicated BLTP3-
914 mRFP constructs (magenta) and LAMP1-GFP (green). Individual channels are shown as inverted
915 grays. Scale bar, 1 µm.
916 **(E)** Ribbon representation of the AlphaFold prediction of a.a. 1-336 of BLTP3A. Blue indicates
917 loops connecting adjoining RBG motifs, and gray indicates the first beta-stand of the third RBG
918 motif.
919 **(F)** Fluorescence images (inverted grays) of RPE-1 cells expressing BLTP3A-1-336-mRFP and
920 either (not shown) GFP-Rab7 (left), or GFP-Rab7 T22N (right). Scale bar, 5 µm. A zoom of an
921 area of the cell at left (dotted square) expressing BLTP3A-1-336-mRFP (magenta) is also shown,
922 along with the Rab7 fluorescence (green), demonstrating the localization of BLTP3A-1-336-
923 mRFP around the entire profile of lysosomes. Individual channels are shown as inverted grays.
924 Scale bar, 2 µm.
925 **(G)** Cartoon depicting the proposed association of BLTP3A vesicle clusters with the surface of
926 lysosomes and the dependence of this association on Rab7.
927
928 **Figure 3: The C terminus of BLTP3A associates with vesicles**
929
930 **(A)** Top: Linear representation of BLTP3A RBG organization and C-terminal truncations indicated
931 by arrows. Bottom left: AlphaFold-based structure of the C terminus of BLTP3A channel.
932 Individual residues are colored by conservation scores as Fig. 1A. Truncations are indicated by
933 arrows. Bottom right: Fluorescence images (inverted grays) of RPE-1 cells expressing the
934 indicated BLTP3A-mRFP constructs along with dominant negative Rab7 (not shown)
935 demonstrating that the property of BLTP3A to bind and cluster vesicles is dependent on its region

936 comprised between a.a. 1327 and 1364. Note that the construct 1-1327, shows a focal
937 accumulation next to the nucleus, which is VAMP7 negative, likely reflecting its pool bound to
938 Rab45 (see Supplemental Figure 1A). Scale bar, 5 µm. Zoomed images (dotted squares) are
939 shown below the main field along with VAMP7 fluorescence. Scale bar, 1 µm.
940 **(B)** Western blots of cell extracts (inputs) of control and edited A549 cells, and of material
941 immunoisolated from these extracts by anti-V5 magnetic beads. Immunolabeling for BLTP3A, V5
942 (endogenously tagged BLTP3A), and for GAPDH as a loading control, are shown.
943 **(C)** Scatter plot of mass spectrometry-identified proteins in immunoisolated material from either
944 control or endogenously edited BLTP3A^V5 A549 cells using anti-V5 magnetic beads. Proteins
945 significantly enriched in material immunoisolated form edited cells compared to wild type cells are
946 plotted in the right-top quadrant. Proteins of note are labeled in magenta.
947
948 **Figure 4: Exogenous BLTP3A is shed from the surface of lysosomes upon damage of their**
949 **membranes.**
950
951 **(A)** Time-series of live fluorescence images (inverted grays) of exogenous BLTP3A-GFP and
952 mApple-IST1 before and after addition of LLOMe. Arrowheads (magenta) point to BLTP3A
953 accumulations shed from lysosomes upon addition of LLOMe. Scale bar, 5 µm.
954 **(B)** Time-series of live fluorescence images of BLTP3A-1-336-mRFP (magenta) and the
955 lysosomal marker NPC1-GFP (green). Fluorescence of individual channels is shown in inverted
956 grays. Scale bar, 2 µm.
957
958 **Figure 5: Activation of CASM recruits BLTP3A to the surface of damaged lysosomes**
959 **through an interaction with mATG8 proteins.**
960
961 **(A)** Alignment of the region of BLTP3A orthologues from different species centered on the a.a.
962 region required for mATG8 binding in human BLTP3A. The alignment shows a high degree of
963 conservation of the key residues of the LC3-interacting (LIR) motif among several chordates and
964 also observed in flies.
965 **(B)** Live fluorescence images (inverted grays) of RPE-1 cells expressing BLTP3A-mRFP (top) or
966 GFP-LC3B (bottom) in either fed (left) or starved (right) conditions. Arrows (magenta) indicate
967 GFP-LC3B positive foci. Scale bar, 5 µm.
968 **(C)** Time-series of live fluorescence images (inverted grays) of exogenous BLTP3A-mRFP and
969 GFP-LC3B before and after addition of LLOMe. Arrowheads point to lysosomes where BLTP3A
970 and LC3B decorate the entire lysosome profile upon addition of LLOMe. Scale bar, 5 µm.
971 **(D)** Time-series of live fluorescence images (inverted grays) of exogenous BLTP3AΔLIR-mRFP
972 and GFP-LC3B before and after addition of LLOMe. Arrowheads point to lysosomes where LC3B,
973 but not BLTP3A lacking a LIR motif, decorates the entire lysosome profile upon addition of
974 LLOMe. Scale bar, 5 µm.
975 **(E)** Correlative fluorescence-FIB-SEM microscopy of GFP-LC3B and BLTP3A-mRFP-positive
976 lysosomes in an RPE-1 cell 15 min after LLOMe addition. Left: Florescence image of an RPE-1
977 cell expressing GFP-LC3B (green), BLTP3A-mRFP (magenta), and mito-BFP (not shown), 15
978 min after addition of LLOMe. Scale bar, 5 µm. Region of cell for FIB-SEM marked by dotted line.
979 Middle: High magnification of the RPE-1 cell at left (blue square) showing both the BLTP3A-mRFP

980 (magenta) and the GFP-LC3B (green) channels. Individual channels are shown as inverted grays.
981 Merged channel also shows mito-BFP (blue) used for aligning EM and fluorescence images.
982 Scale bar, 2 μm. Right: EM reconstruction (scale bar, 1 μm) corresponding to the blue square
983 from left. Lysosome, dark green; ER, yellow; mitochondria, blue; small vesicles, magenta.
984 **(F)** Hypothetical model illustrating the different organization and orientation of BLTP3A on the
985 surface of lysosomes depending on the state of the cell.
986
987 **Figure 6: LC3-dependent BLTP3A recruitment to vacuoles containing internalized MSU**
988 **crystals via CASM activation.**
989 **(A)** Brightfield image of RPE-1 cells incubated with MSU crystals (200ug/mL) for 2 hrs.
990 Arrowheads indicate MSU crystals. Scale bars, 5 μm.
991 **(B)** Live fluorescence images of RPE-1 cells expressing BLTP3A-mRFP and LAMP1-GFP (shown
992 as inverted greys) and incubated with MSU crystals for 2 hrs. Scale bar, 5 μm. Zoomed images
993 (dotted rectangles) of individual channels are shown to the right. Scale bars, 2 μm. Arrowheads
994 point to the surface of crystal-containing vacuoles positive for BLTP3A-mRFP and LAMP1-GFP.
995 **(C)** Live fluorescence images of RPE-1 cells co-expressing either BLTP3A-mRFP (top row) or
996 BLTP3AΔLIR-mRFP (bottom row) with GFP-LC3B and incubated with MSU crystals for 2 hrs.
997 Individual channels are shown as inverted greys. Scale bar, 10 μm. Zoomed images (dotted
998 rectangles) of individual channels are shown to the right. Scale bar, 2 μm. Arrowheads point to
999 the surface of the crystal-containing vacuoles positive for GFP-LC3B to highlight the presence of
1000 BLTP3A-mRFP (top) and the absence of BLTP3AΔLIR-mRFP (bottom).
1001 **(D)** Time-series of live fluorescence images (inverted grays) of BLTP3A-mRFP and GFP-LC3B in
1002 RPE-1 cells incubated with MSU crystals. Scale bar, 2 μm. Arrowheads point to the surface of
1003 crystal-containing vacuoles.
1004
1005 **Figure7: Lysosomes are more susceptible to damage in cells lacking BLTP3A**
1006
1007 **(A)** Western blots of cell extracts (inputs) of control and edited A549 cells (BLTP3A KO clones)
1008 for the proteins indicated.
1009 **(B)** Fluorescence images of parental control (left) or BLTP3A KO (right) A549 cells with antibodies
1010 against LAMP1 (green). Scale bar, 20 μm.
1011 **(C)** Fluorescence images of parental control (top row) or BLTP3A KO (bottom row) A549 cells
1012 with antibodies against galectin-3 (inverted greys). Cells were treated with vehicle control (left
1013 column) or 1mM LLOMe (right column).
1014 **(D)** Quantification of galectin-3 spots per cell from field **C**. Error bars report the standard error of
1015 the mean (SEM). **, $p < 0.01$. Mean number of galectin-3 spots per cell and number of cells
1016 counted per condition indicated.
1017
1018 **SUPPLEMENTAL FIGURE LEGENDS**
1019
1020 **Supplemental Figure 1**
1021

(A) Live fluorescence images (inverted grays) of RPE-1 cells expressing either GFP-Rab45 (left), BLTP3A-mRFP (center), or both proteins together (only BLTP3A is shown) (right) as indicated. Scale bar, 5 µm. High-magnification scale bar, 2 µm.
(B) Genomic sequence of the edited BLTP3A locus (insertion of the V5 epitope) in A549 cell. Blue, small Gly-Ser linkers; green, V5 epitope sequence.
(C) AlphaFold prediction of BLTP3A. The site where the V5 epitope (V904) was inserted is indicated. The long disordered sequence and the C-terminal helix are shown in gray.
(D) Left: Fluorescence image of an RPE-1 cell expressing exogenous BLTP3B-mRFP (inverted grays) and immunolabeled with antibodies against endogenous VAMP7 (shown at right in the high magnification of the squared region in the main field). Scale bar, 5 µm. Right: zooms of different RPE-1 cells expressing exogenous BLTP3B-mRFP (magenta) and immunolabeled with antibodies (green) against endogenous VAMP4 or ATG9A. Individual channels are shown as inverted grays. Merge of channels on bottom. Scale bar, 1 µm.
(E) Fluorescence images of RPE-1 cells expressing the indicated BLTP3A-mRFP construct. Scale bar, 5 µm.
(F) Live fluorescence images (inverted grays) of RPE-1 cells expressing exogenous GFP-LRRK1^{K746G} (left) and BLTP3A-mRFP (right). Scale bar, 10 µm.
(G) Western blot of lysate of RPE-1 cells expressing exogenous RFP-LRRK1^{K746G} or RFP-LRRK1^{D1409A} for RFP (to detect LRRK1 fusions), Rab7, phospho-Rab7 S72, and alpha-tubulin as a loading control.

Supplemental Figure 2

(A) AlphaFold3 multimer prediction of full-length MAP1LC3B (green) and a.a. 1110-1150 of BLTP3A (magenta). Arrows indicate key residues of the LIR motif of BLTP3A.
(B) AlphaFold3 multimer predictions of mATG8 proteins and a.a. 1110-1150 of BLTP3A with and without the LIR motif (ΔLIR).
(C) Time-series of live fluorescence images (inverted grays) of BLTP3A-mRFP and GFP-LC3B before and after addition of GPN. Arrowheads point to lysosomes where BLTP3A and LC3B decorate the entire profile upon addition of GPN. Time, seconds. Scale bar, 5 µm.
(D) Genomic sequence of the edited BLTP3A locus in A549 cell. Blue, gRNA; green, PAM; red, indel mutations.
(E) Quantification of relative LAMP1 expression from western blots (n=3) of Figure 7A. Error bars indicate the standard error of the mean (SEM).

Supplemental Movie 1
FIB-SEM reconstruction of GFP-LC3B and BLTP3A-mRFP-positive lysosomes in an RPE-1 cell 15 min after LLOMe addition (from Figure 5E). Reconstructed organelle colors: lysosome, dark green; ER, yellow; mitochondria, blue; small vesicles, magenta; large vesicles, green. Scale bar, 1 µm.

Supplemental Movie 2
FIB-SEM image stack of the region used for the reconstruction in Figure 5E and Supplemental Movie 1. Lysosomes are pseudo-colored dark green. Scale bar, 1 µm.

REFERENCES

Abramson, J., J. Adler, J. Dunger, R. Evans, T. Green, A. Pritzel, O. Ronneberger, L. Willmore, A.J. Ballard, J. Bambrick, S.W. Bodenstein, D.A. Evans, C.-C. Hung, M. O'Neill, D. Reiman, K. Tunyasuvunakool, Z. Wu, A. Žemgulytė, E. Arvaniti, C. Beattie, O. Bertolli, A. Bridgland, A. Cherepanov, M. Congreve, A.I. Cowen-Rivers, A. Cowie, M. Figurnov, F.B. Fuchs, H. Gladman, R. Jain, Y.A. Khan, C.M.R. Low, K. Perlin, A. Potapenko, P. Savy, S. Singh, A. Stecula, A. Thillaisundaram, C. Tong, S. Yakneen, E.D. Zhong, M. Zielinski, A. Žídek, V. Bapst, P. Kohli, M. Jaderberg, D. Hassabis, and J.M. Jumper. 2024. Accurate structure prediction of biomolecular interactions with AlphaFold 3. *Nature*. 630:493–500. doi:10.1038/s41586-024-07487-w.

Adlakha, J., Z. Hong, P. Li, and K.M. Reinisch. 2022. Structural and biochemical insights into lipid transport by VPS13 proteins. *Journal of Cell Biology*. 221:e202202030. doi:10.1083/jcb.202202030.

Advani, R.J., B. Yang, R. Prekeris, K.C. Lee, J. Klumperman, and R.H. Scheller. 1999. Vamp-7 Mediates Vesicular Transport from Endosomes to Lysosomes. *Journal of Cell Biology*. 146:765–776. doi:10.1083/jcb.146.4.765.

Anding, A.L., C. Wang, T.-K. Chang, D.A. Sliter, C.M. Powers, K. Hofmann, R.J. Youle, and E.H. Baehrecke. 2018. Vps13D Encodes a Ubiquitin-Binding Protein that Is Required for the Regulation of Mitochondrial Size and Clearance. *Current Biology*. 28:287-295.e6. doi:10.1016/j.cub.2017.11.064.

Armon, A., D. Graur, and N. Ben-Tal. 2001. ConSurf: an algorithmic tool for the identification of functional regions in proteins by surface mapping of phylogenetic information1. *Journal of Molecular Biology*. 307:447–463. doi:10.1006/jmbi.2000.4474.

Bahadoran, P., E. Aberdam, F. Mantoux, R. Buscà, K. Bille, N. Yalman, G. de Saint-Basile, R. Casaroli-Marano, J.-P. Ortonne, and R. Ballotti. 2001. Rab27a: A Key to Melanosome Transport in Human Melanocytes. *Journal of Cell Biology*. 152:843–850. doi:10.1083/jcb.152.4.843.

Baldwin, H.A., C. Wang, G. Kanfer, H.V. Shah, A. Velayos-Baeza, M. Dulovic-Mahlow, N. Brüggemann, A. Anding, E.H. Baehrecke, D. Maric, W.A. Prinz, and R.J. Youle. 2021. VPS13D promotes peroxisome biogenesis. *Journal of Cell Biology*. 220:e202001188. doi:10.1083/jcb.202001188.

Banerjee, S., S. Daetwyler, X. Bai, M. Michaud, J. Jouhet, S. Madhugiri, E. Johnson, C.-W. Wang, R. Fiolka, A. Toulmay, and W.A. Prinz. 2024. The Vps13-like protein BLTP2 is pro-survival and regulates phosphatidylethanolamine levels in the plasma membrane to maintain its fluidity and function. 2024.02.04.578804. doi:10.1101/2024.02.04.578804.

Bentley-DeSousa, A., and S.M. Ferguson. 2023. A STING-CASM-GABARAP Pathway Activates LRRK2 at Lysosomes. 2023.10.31.564602. doi:10.1101/2023.10.31.564602.

Boyle, K.B., C.J. Ellison, P.R. Elliott, M. Schuschnig, K. Grimes, M.S. Dionne, C. Sasakawa, S. Munro, S. Martens, and F. Randow. 2023. TECPR1 conjugates LC3 to damaged endomembranes upon detection of sphingomyelin exposure. *The EMBO Journal*. 42:e113012. doi:10.15252/embj.2022113012.

Cai, S., Y. Wu, A. Guillen-Samander, W. Hancock-Cerutti, J. Liu, and P.D. Camilli. 2022a. In situ architecture of the lipid transport protein VPS13C at ER-lysosomes membrane contacts. 2022.03.08.482579. doi:10.1101/2022.03.08.482579.

Cai, S., Y. Wu, A. Guillén-Samander, W. Hancock-Cerutti, J. Liu, and P. De Camilli. 2022b. In situ architecture of the lipid transport protein VPS13C at ER–lysosome membrane contacts. *Proceedings of the National Academy of Sciences*. 119:e2203769119. doi:10.1073/pnas.2203769119.

Carter, A.P., A.G. Diamant, and L. Urnavicius. 2016. How dynein and dynactin transport cargos: a structural perspective. *Current Opinion in Structural Biology*. 37:62–70. doi:10.1016/j.sbi.2015.12.003.

Chen, W., M.M. Motsinger, J. Li, K.P. Bohannon, and P.I. Hanson. 2024. Ca2+-sensor ALG-2 engages ESCRTs to enhance lysosomal membrane resilience to osmotic stress. *Proceedings of the National Academy of Sciences*. 121:e2318412121. doi:10.1073/pnas.2318412121.

Cohen, S., A.M. Valm, and J. Lippincott-Schwartz. 2018. Interacting organelles. *Current Opinion in Cell Biology*. 53:84–91. doi:10.1016/j.ceb.2018.06.003.

Corkery, D.P., S. Castro-Gonzalez, A. Knyazeva, L.K. Herzog, and Y. Wu. 2023. An ATG12-ATG5-TECPR1 E3-like complex regulates unconventional LC3 lipidation at damaged lysosomes. *EMBO reports*. 24:e56841. doi:10.15252/embr.202356841.

Corkery, D.P., S. Li, D. Wijayatunga, L.K. Herzog, A. Knyazeva, and Y.-W. Wu. 2024. ESCRT recruitment to damaged lysosomes is dependent on the ATG8 E3-like ligases. 2024.04.30.591897. doi:10.1101/2024.04.30.591897.

Cross, J., J. Durgan, D.G. McEwan, M. Tayler, K.M. Ryan, and O. Florey. 2023. Lysosome damage triggers direct ATG8 conjugation and ATG2 engagement via non-canonical autophagy. *Journal of Cell Biology*. 222:e202303078. doi:10.1083/jcb.202303078.

De Camilli, P., F. Benfenati, F. Valtorta, and P. Greengard. 1990. The Synapsins. *Annual Review of Cell and Developmental Biology*. 6:433–460. doi:10.1146/annurev.cb.06.110190.002245.

DeGrella, R.F., and R.D. Simoni. 1982. Intracellular transport of cholesterol to the plasma membrane. *Journal of Biological Chemistry*. 257:14256–14262. doi:10.1016/S0021-9258(19)45374-X.

Deretic, V., T. Duque, E. Trosdal, M. Paddar, R. Javed, and P. Akepati. 2024. Membrane atg8ylation in Canonical and Noncanonical Autophagy. *Journal of Molecular Biology*. 436:168532. doi:10.1016/j.jmb.2024.168532.

Durgan, J., and O. Florey. 2022. Many roads lead to CASM: Diverse stimuli of noncanonical autophagy share a unifying molecular mechanism. *Science Advances*. 8:eabo1274. doi:10.1126/sciadv.abo1274.

1146 Dziurdzik, S.K., and E. Conibear. 2021. The Vps13 Family of Lipid Transporters and Its Role at
1147 Membrane Contact Sites. *International Journal of Molecular Sciences*. 22:2905.
1148 doi:10.3390/ijms22062905.

1149 Figueras-Novoa, C., L. Timimi, E. Marcassa, R. Ulferts, and R. Beale. 2024. Conjugation of
1150 ATG8s to single membranes at a glance. *Journal of Cell Science*. 137:jcs261031.
1151 doi:10.1242/jcs.261031.

1152 Fischer, T.D., C. Wang, B.S. Padman, M. Lazarou, and R.J. Youle. 2020. STING induces LC3B
1153 lipidation onto single-membrane vesicles via the V-ATPase and ATG16L1-WD40 domain.
1154 *Journal of Cell Biology*. 219:e202009128. doi:10.1083/jcb.202009128.

1155 Fujita, K., S. Kedashiro, T. Yagi, N. Hisamoto, K. Matsumoto, and H. Hanafusa. 2022. The ULK
1156 complex–LRRK1 axis regulates Parkin-mediated mitophagy via Rab7 Ser-72
1157 phosphorylation. *Journal of Cell Science*. 135:jcs260395. doi:10.1242/jcs.260395.

1158 Gateva, V., J.K. Sandling, G. Hom, K.E. Taylor, S.A. Chung, X. Sun, W. Ortmann, R. Kosoy, R.C.
1159 Ferreira, G. Nordmark, I. Gunnarsson, E. Svenungsson, L. Padyukov, G. Sturfelt, A.
1160 Jönsen, A.A. Bengtsson, S. Rantapää-Dahlqvist, E.C. Baechler, E.E. Brown, G.S.
1161 Alarcón, J.C. Edberg, R. Ramsey-Goldman, G. McGwin, J.D. Reveille, L.M. Vilá, R.P.
1162 Kimberly, S. Manzi, M.A. Petri, A. Lee, P.K. Gregersen, M.F. Seldin, L. Rönnblom, L.A.
1163 Criswell, A.-C. Syvänen, T.W. Behrens, and R.R. Graham. 2009. A large-scale replication
1164 study identifies TNIP1, PRDM1, JAZF1, UHRF1BP1 and IL10 as risk loci for systemic
1165 lupus erythematosus. *Nat Genet*. 41:1228–1233. doi:10.1038/ng.468.

1166 Gillingham, A.K., J. Bertram, F. Begum, and S. Munro. 2019. In vivo identification of GTPase
1167 interactors by mitochondrial relocalization and proximity biotinylation. *eLife*. 8:e45916.
1168 doi:10.7554/eLife.45916.

1169 Goldman, R., and A. Kaplan. 1973. Rupture of rat liver lysosomes mediated by l-amino acid
1170 esters. *Biochimica et Biophysica Acta (BBA) - Biomembranes*. 318:205–216.
1171 doi:10.1016/0005-2736(73)90114-4.

1172 Gómez-Sánchez, R., J. Rose, R. Guimarães, M. Mari, D. Papinski, E. Rieter, W.J. Geerts, R.
1173 Hardenberg, C. Kraft, C. Ungermann, and F. Reggiori. 2018. Atg9 establishes Atg2-
1174 dependent contact sites between the endoplasmic reticulum and phagophores. *The*
1175 *Journal of cell biology*. jcb.201710116. doi:10.1083/jcb.201710116.

1176 Guillén-Samander, A., M. Leonzino, M.G. Hanna IV, N. Tang, H. Shen, and P. De Camilli. 2021.
1177 VPS13D bridges the ER to mitochondria and peroxisomes via Miro. *Journal of Cell*
1178 *Biology*. 220. doi:10.1083/jcb.202010004.

1179 Guillén-Samander, A., Y. Wu, S.S. Pineda, F.J. García, J.N. Eisen, M. Leonzino, B. Ugur, M.
1180 Kellis, M. Heiman, and P. De Camilli. 2022. A partnership between the lipid scramblase
1181 XK and the lipid transfer protein VPS13A at the plasma membrane. *Proceedings of the*
1182 *National Academy of Sciences*. 119:e2205425119. doi:10.1073/pnas.2205425119.

1183 Hanna, M., A. Guillén-Samander, and P. De Camilli. 2023. RBG Motif Bridge-Like Lipid Transport
1184 Proteins: Structure, Functions, and Open Questions. *Annu. Rev. Cell Dev. Biol.*
1185 doi:10.1146/annurev-cellbio-120420-014634.

1186 Hanna, M.G., P.H. Suen, Y. Wu, K.M. Reinisch, and P. De Camilli. 2022. SHIP164 is a chorein
1187 motif lipid transfer protein that controls endosome–Golgi membrane traffic. *Journal of Cell*
1188 *Biology*. 221:e202111018. doi:10.1083/jcb.202111018.

1189 Heo, J.-M., A. Ordureau, S. Swarup, J.A. Paulo, K. Shen, D.M. Sabatini, and J.W. Harper. 2018.
1190 RAB7A phosphorylation by TBK1 promotes mitophagy via the PINK-PARKIN pathway.
1191 *Science Advances*. 4:eaav0443. doi:10.1126/sciadv.aav0443.

1192 Herbst, S., P. Campbell, J. Harvey, E.M. Bernard, V. Papayannopoulos, N.W. Wood, H.R. Morris,
1193 and M.G. Gutierrez. 2020. LRRK2 activation controls the repair of damaged
1194 endomembranes in macrophages. *The EMBO Journal*. 39:e104494.
1195 doi:10.15252/embj.2020104494.

1196 Hume, A.N., L.M. Collinson, A. Rapak, A.Q. Gomes, C.R. Hopkins, and M.C. Seabra. 2001.
1197 Rab27a Regulates the Peripheral Distribution of Melanosomes in Melanocytes. *Journal of*
1198 *Cell Biology*. 152:795–808. doi:10.1083/jcb.152.4.795.

1199 John Peter, A.T., B. Herrmann, D. Antunes, D. Rapaport, K.S. Dimmer, and B. Kornmann. 2017.
1200 Vps13-Mcp1 interact at vacuole–mitochondria interfaces and bypass ER–mitochondria
1201 contact sites. *J Cell Biol*. 216:3219–3229. doi:10.1083/jcb.201610055.

1202 John Peter, A.T., S.N.S. van Schie, N.J. Cheung, A.H. Michel, M. Peter, and B. Kornmann. 2022.
1203 Rewiring phospholipid biosynthesis reveals resilience to membrane perturbations and
1204 uncovers regulators of lipid homeostasis. *The EMBO Journal*. 41:e109998.
1205 doi:10.15252/embj.2021109998.

1206 Johnston, P.A., R. Jahn, and T.C. Südhof. 1989. Transmembrane Topography and Evolutionary
1207 Conservation of Synaptophysin. *Journal of Biological Chemistry*. 264:1268–1273.
1208 doi:10.1016/S0021-9258(19)85081-0.

1209 Jumper, J., R. Evans, A. Pritzel, T. Green, M. Figurnov, O. Ronneberger, K. Tunyasuvunakool,
1210 R. Bates, A. Žídek, A. Potapenko, A. Bridgland, C. Meyer, S.A.A. Kohl, A.J. Ballard, A.
1211 Cowie, B. Romera-Paredes, S. Nikolov, R. Jain, J. Adler, T. Back, S. Petersen, D. Reiman,
1212 E. Clancy, M. Zielinski, M. Steinegger, M. Pacholska, T. Berghammer, S. Bodenstein, D.
1213 Silver, O. Vinyals, A.W. Senior, K. Kavukcuoglu, P. Kohli, and D. Hassabis. 2021. Highly
1214 accurate protein structure prediction with AlphaFold. *Nature*. 596:583–589.
1215 doi:10.1038/s41586-021-03819-2.

1216 Kang, Y., K.S. Lehmann, J. Vanegas, H. Long, A. Jefferson, M.A. Freeman, and S. Clark. 2024.
1217 Structural basis of bulk lipid transfer by bridge-like lipid transfer protein LPD-3.
1218 2024.06.21.600134. doi:10.1101/2024.06.21.600134.

1219 Kaur, N., L.R. de la Ballina, H.S. Haukaas, M.L. Torgersen, M. Radulovic, M.J. Munson, A.
1220 Sabirsh, H. Stenmark, A. Simonsen, S.R. Carlsson, and A.H. Lystad. 2023. TECPR1 is
1221 activated by damage-induced sphingomyelin exposure to mediate
1222 noncanonical autophagy. *The EMBO Journal*. 42:e113105.
1223 doi:10.15252/embj.2022113105.

1224 Kumar, N., M. Leonzino, W. Hancock-Cerutti, F.A. Horenkamp, P. Li, J.A. Lees, H. Wheeler, K.M.
1225 Reinisch, and P.D. Camilli. 2018. VPS13A and VPS13C are lipid transport proteins

1226 differentially localized at ER contact sites. *The Journal of cell biology*. 217:3625–3639.
1227 doi:10.1083/jcb.201807019.

1228 Leonzino, M., K.M. Reinisch, and P. De Camilli. 2021. Insights into VPS13 properties and function
1229 reveal a new mechanism of eukaryotic lipid transport. *Biochimica et Biophysica Acta*
1230 *(BBA) - Molecular and Cell Biology of Lipids*. 1866:159003.
1231 doi:10.1016/j.bbalip.2021.159003.

1232 Levine, T.P. 2019. Remote homology searches identify bacterial homologues of eukaryotic lipid
1233 transfer proteins, including Chorein-N domains in TamB and AsmA and Mdm31p. *BMC*
1234 *Molecular and Cell Biology*. 20. doi:10.1186/s12860-019-0226-z.

1235 Levine, T.P. 2022. Sequence Analysis and Structural Predictions of Lipid Transfer Bridges in the
1236 Repeating Beta Groove (RBG) Superfamily Reveal Past and Present Domain Variations
1237 Affecting Form, Function and Interactions of VPS13, ATG2, SHIP164, Hobbit and Tweek.
1238 *Contact*. 5:25152564221134328. doi:10.1177/25152564221134328.

1239 Li, P., J.A. Lees, C.P. Lusk, and K.M. Reinisch. 2020. Cryo-EM reconstruction of a VPS13
1240 fragment reveals a long groove to channel lipids between membranes. *Journal of Cell*
1241 *Biology*. 219. doi:10.1083/jcb.202001161.

1242 Lin, S.X., W.G. Mallet, A.Y. Huang, and F.R. Maxfield. 2003. Endocytosed Cation-Independent
1243 Mannose 6-Phosphate Receptor Traffics via the Endocytic Recycling Compartment en
1244 Route to the trans-Golgi Network and a Subpopulation of Late Endosomes. *MBoC*.
1245 15:721–733. doi:10.1091/mbc.e03-07-0497.

1246 Maeda, S., C. Otomo, and T. Otomo. 2019. The autophagic membrane tether ATG2A transfers
1247 lipids between membranes. *eLife*. 8:e45777. doi:10.7554/eLife.45777.

1248 Mallard, F., B.L. Tang, T. Galli, D. Tenza, A. Saint-Pol, X. Yue, C. Antony, W. Hong, B. Goud, and
1249 L. Johannes. 2002. Early/recycling endosomes-to-TGN transport involves two SNARE
1250 complexes and a Rab6 isoform. *The Journal of cell biology*. 156:653–664.
1251 doi:10.1083/jcb.200110081.

1252 Martinez-Arca, S., S. Coco, G. Mainguy, U. Schenk, P. Alberts, P. Bouillé, M. Mezzina, A.
1253 Prochiantz, M. Matteoli, D. Louvard, and T. Galli. 2001. A Common Exocytotic Mechanism
1254 Mediates Axonal and Dendritic Outgrowth. *J. Neurosci.* 21:3830–3838.
1255 doi:10.1523/JNEUROSCI.21-11-03830.2001.

1256 Melia, T.J., A.H. Lystad, and A. Simonsen. 2020. Autophagosome biogenesis: From membrane
1257 growth to closure. *Journal of Cell Biology*. 219:e202002085. doi:10.1083/jcb.202002085.

1258 Ménasché, G., E. Pastural, J. Feldmann, S. Certain, F. Ersoy, S. Dupuis, N. Wulffraat, D. Bianchi,
1259 A. Fischer, F. Le Deist, and G. de Saint Basile. 2000. Mutations in RAB27A cause Griscelli
1260 syndrome associated with haemophagocytic syndrome. *Nat Genet*. 25:173–176.
1261 doi:10.1038/76024.

1262 Meyer, H., and B. Kravic. 2024. The Endo-Lysosomal Damage Response. *Annual Review of*
1263 *Biochemistry*. 93:367–387. doi:10.1146/annurev-biochem-030222-102505.

1264 Milovanovic, D., and P. De Camilli. 2017. Synaptic Vesicle Clusters at Synapses: A Distinct Liquid
1265 Phase? *Neuron*. 93:995–1002. doi:10.1016/j.neuron.2017.02.013.

1266 Milovanovic, D., Y. Wu, X. Bian, and P. De Camilli. 2018. A liquid phase of synapsin and lipid
1267 vesicles. *Science*. 361:604–607. doi:10.1126/science.aat5671.

1268 Nagashima, K., S. Torii, Z. Yi, M. Igarashi, K. Okamoto, T. Takeuchi, and T. Izumi. 2002.
1269 Melanophilin directly links Rab27a and myosin Va through its distinct coiled-coil regions.
1270 *FEBS Letters*. 517:233–238. doi:10.1016/S0014-5793(02)02634-0.

1271 Nagata, K., T. Satoh, H. Itoh, T. Kozasa, Y. Okano, T. Doi, Y. Kaziro, and Y. Nozawa. 1990. The
1272 ram: A novel low molecular weight GTP-binding protein cDNA from a rat megakaryocyte
1273 library. *FEBS Letters*. 275:29–32. doi:10.1016/0014-5793(90)81431-M.

1274 Neuman, S.D., T.P. Levine, and A. Bashirullah. 2022. A novel superfamily of bridge-like lipid
1275 transfer proteins. *Trends in Cell Biology*. 32:962–974. doi:10.1016/j.tcb.2022.03.011.

1276 Nieto-Torres, J.L., A.M. Leidal, J. Debnath, and M. Hansen. 2021. Beyond Autophagy: The
1277 Expanding Roles of ATG8 Proteins. *Trends in Biochemical Sciences*. 46:673–686.
1278 doi:10.1016/j.tibs.2021.01.004.

1279 Nirujogi, R.S., F. Tonelli, M. Taylor, P. Lis, A. Zimprich, E. Sammler, and D.R. Alessi. 2021.
1280 Development of a multiplexed targeted mass spectrometry assay for LRRK2-
1281 phosphorylated Rabs and Ser910/Ser935 biomarker sites. *Biochemical Journal*. 478:299–
1282 326. doi:10.1042/BCJ20200930.

1283 Osawa, T., T. Kotani, T. Kawaoka, E. Hirata, K. Suzuki, H. Nakatogawa, Y. Ohsumi, and N.N.
1284 Noda. 2019. Atg2 mediates direct lipid transfer between membranes for autophagosome
1285 formation. *Nat Struct Mol Biol*. 26:281–288. doi:10.1038/s41594-019-0203-4.

1286 Otto, G.P., M. Razi, J. Morvan, F. Stenner, and S.A. Tooze. 2010. A novel syntaxin 6-interacting
1287 protein, SHIP164, regulates syntaxin 6-dependent sorting from early endosomes. *Traffic*
1288 *(Copenhagen, Denmark)*. 11:688–705. doi:10.1111/j.1600-0854.2010.01049.x.

1289 Palade, G. 1975. Intracellular Aspects of the Process of Protein Synthesis. *Science*. 189:347–
1290 358. doi:10.1126/science.1096303.

1291 Pang, S., and C.S. Xu. 2023. Chapter 11 - Methods of enhanced FIB-SEM sample preparation
1292 and image acquisition. K. Narayan, L. Collinson, and P. Verkade, editors. Academic Press.

1293 Park, D., Y. Wu, S.-E. Lee, G. Kim, S. Jeong, D. Milovanovic, P. De Camilli, and S. Chang. 2021.
1294 Cooperative function of synaptophysin and synapsin in the generation of synaptic vesicle-
1295 like clusters in non-neuronal cells. *Nat Commun*. 12:263. doi:10.1038/s41467-020-20462-
1296 z.

1297 Park, J.-S., and A.M. Neiman. 2012. VPS13 regulates membrane morphogenesis during
1298 sporulation in Saccharomyces cerevisiae. *Journal of Cell Science*. 125:3004–3011.
1299 doi:10.1242/jcs.105114.

1300 Park, J.-S., M.K. Thorsness, R. Policastro, L.L. McGoldrick, N.M. Hollingsworth, P.E. Thorsness,
1301 and A.M. Neiman. 2016. Yeast Vps13 promotes mitochondrial function and is localized at
1302 membrane contact sites. *MBoC*. 27:2435–2449. doi:10.1091/mbc.E16-02-0112.

1303 Pols, M.S., E. van Meel, V. Oorschot, C. ten Brink, M. Fukuda, M.G. Swetha, S. Mayor, and J.
1304 Klumperman. 2013. hVps41 and VAMP7 function in direct TGN to late endosome
1305 transport of lysosomal membrane proteins. *Nat Commun*. 4:1361.
1306 doi:10.1038/ncomms2360.

1307 Prinz, W.A., A. Toulmay, and T. Balla. 2020. The functional universe of membrane contact sites.
1308 *Nature Reviews Molecular Cell Biology*. 21:7–24. doi:10.1038/s41580-019-0180-9.

1309 Radulovic, M., K.O. Schink, E.M. Wenzel, V. Nähse, A. Bongiovanni, F. Lafont, and H. Stenmark.
1310 2018. ESCRT-mediated lysosome repair precedes lysophagy and promotes cell survival.
1311 *The EMBO Journal*. 37:e99753. doi:10.15252/embj.201899753.

1312 Radulovic, M., E.M. Wenzel, S. Gilani, L.K. Holland, A.H. Lystad, S. Phuyal, V.M. Olkkonen, A.
1313 Brech, M. Jäättelä, K. Maeda, C. Raiborg, and H. Stenmark. 2022. Cholesterol transfer
1314 via endoplasmic reticulum contacts mediates lysosome damage repair. *The EMBO*
1315 *Journal*. 41:e112677. doi:10.15252/embj.2022112677.

1316 Reinisch, K., P. De Camilli, and T. Melia. 2024. Lipid dynamics at membrane contact sites. *Annu.*
1317 *Rev. Biochem.*

1318 Rogov, V.V., Nezis ,Ioannis P., Tsapras ,Panagiotis, Zhang ,Hong, Dagdas ,Yasin, Noda ,Nobuo
1319 N., Nakatogawa ,Hitoshi, Wirth ,Martina, Mouilleron ,Stephane, McEwan ,David G.,
1320 Behrends ,Christian, Deretic ,Vojo, Elazar ,Zvulun, Tooze ,Sharon A., Dikic ,Ivan, Lamark
1321 ,Trond, and T. and Johansen. 2023. Atg8 family proteins, LIR/AIM motifs and other
1322 interaction modes. *Autophagy Reports*. 2:2188523.
1323 doi:10.1080/27694127.2023.2188523.

1324 Saheki, Y., and P.D. Camilli. 2017. Endoplasmic Reticulum-Plasma Membrane Contact Sites.
1325 *Annual review of biochemistry*. 86:659–684. doi:10.1146/annurev-biochem-061516-
1326 044932.

1327 Scorrano, L., M.A. De Matteis, S. Emr, F. Giordano, G. Hajnóczky, B. Kornmann, L.L. Lackner,
1328 T.P. Levine, L. Pellegrini, K. Reinisch, R. Rizzuto, T. Simmen, H. Stenmark, C.
1329 Ungermann, and M. Schuldiner. 2019. Coming together to define membrane contact sites.
1330 *Nat Commun*. 10:1287. doi:10.1038/s41467-019-09253-3.

1331 Shukla, S., K.P. Larsen, C. Ou, K. Rose, and J.H. Hurley. 2022. In vitro reconstitution of calcium-
1332 dependent recruitment of the human ESCRT machinery in lysosomal membrane repair.
1333 *Proceedings of the National Academy of Sciences*. 119:e2205590119.
1334 doi:10.1073/pnas.2205590119.

1335 Skowyra, M.L., P.H. Schlesinger, T.V. Naismith, and P.I. Hanson. 2018. Triggered recruitment of
1336 ESCRT machinery promotes endolysosomal repair. *Science*. 360:eaar5078.
1337 doi:10.1126/science.aar5078.

1338 Stenmark, H., and V.M. Olkkonen. 2001. The Rab GTPase family. *Genome Biology*.
1339 2:reviews3007.1. doi:10.1186/gb-2001-2-5-reviews3007.

1340 Strom, M., A.N. Hume, A.K. Tarafder, E. Barkagianni, and M.C. Seabra. 2002. A Family of Rab27-
1341 binding Proteins: MELANOPHILIN LINKS Rab27a AND MYOSIN Va FUNCTION IN
1342 MELANOSOME TRANSPORT*. *Journal of Biological Chemistry*. 277:25423–25430.
1343 doi:10.1074/jbc.M202574200.

1344 Südhof, T.C., A.J. Czernik, H.-T. Kao, K. Takei, P.A. Johnston, A. Horiuchi, S.D. Kanazir, M.A.
1345 Wagner, M.S. Perin, P. De Camilli, and P. Greengard. 1989. Synapsins: Mosaics of
1346 Shared and Individual Domains in a Family of Synaptic Vesicle Phosphoproteins. *Science*.
1347 245:1474–1480. doi:10.1126/science.2506642.

1348 Talaia, G., A. Bentley-DeSousa, and S.M. Ferguson. 2024. Lysosomal TBK1 responds to amino
1349 acid availability to relieve Rab7-dependent mTORC1 inhibition. *The EMBO Journal*. 1–20.
1350 doi:10.1038/s44318-024-00180-8.

1351 Tan, J.X., and T. Finkel. 2022. A phosphoinositide signalling pathway mediates rapid lysosomal
1352 repair. *Nature*. 1–7. doi:10.1038/s41586-022-05164-4.

1353 Thiele, D.L., and P.E. Lipsky. 1990. Mechanism of L-leucyl-L-leucine methyl ester-mediated killing
1354 of cytotoxic lymphocytes: dependence on a lysosomal thiol protease, dipeptidyl peptidase
1355 I, that is enriched in these cells. *Proceedings of the National Academy of Sciences*. 87:83–
1356 87. doi:10.1073/pnas.87.1.83.

1357 Tokai, M., H. Kawasaki, Y. Kikuchi, and K. Ouchi. 2000. Cloning and Characterization of the CSF1
1358 Gene ofSaccharomyces cerevisiae, Which Is Required for Nutrient Uptake at Low
1359 Temperature. *Journal of Bacteriology*. 182:2865–2868. doi:10.1128/JB.182.10.2865-
1360 2868.2000.

1361 Tran, T.H.T., Q. Zeng, and W. Hong. 2007. VAMP4 cycles from the cell surface to the trans-Golgi
1362 network via sorting and recycling endosomes. *Journal of Cell Science*. 120:1028–1041.
1363 doi:10.1242/jcs.03387.

1364 Tu, Y.X., and J. Brumell. 2020. Examining the Autophagy Proximity Interactome. University of
1365 Toronto.

1366 Uchimoto, T., H. Nohara, R. Kamehara, M. Iwamura, N. Watanabe, and Y. Kobayashi. 1999.
1367 Mechanism of apoptosis induced by a lysosomotropic agent, L-Leucyl-L-Leucine methyl
1368 ester. *Apoptosis*. 4:357–362. doi:https://doi.org/10.1023/A:1009695221038.

1369 Unoki, M., T. Nishidate, and Y. Nakamura. 2004. ICBP90, an E2F-1 target, recruits HDAC1 and
1370 binds to methyl-CpG through its SRA domain. *Oncogene*. 23:7601–7610.
1371 doi:10.1038/sj.onc.1208053.

1372 Valverde, D.P., S. Yu, V. Boggavarapu, N. Kumar, J.A. Lees, T. Walz, K.M. Reinisch, and T.J.
1373 Melia. 2019. ATG2 transports lipids to promote autophagosome biogenesis.
1374 *Journal of Cell Biology*. 218:1787–1798. doi:10.1083/jcb.201811139.

1375 Velikkakath, A.K.G., T. Nishimura, E. Oita, N. Ishihara, and N. Mizushima. 2012. Mammalian Atg2
1376 proteins are essential for autophagosome formation and important for regulation of size
1377 and distribution of lipid droplets. *MBoC*. 23:896–909. doi:10.1091/mbc.e11-09-0785.

van Vliet, A.R., G.N. Chiduza, S.L. Maslen, V.E. Pye, D. Joshi, S. De Tito, H.B.J. Jefferies, E. Christodoulou, C. Roustan, E. Punch, J.H. Hervás, N. O'Reilly, J.M. Skehel, P. Cherepanov, and S.A. Tooze. 2022. ATG9A and ATG2A form a heteromeric complex essential for autophagosome formation. *Molecular Cell*. 82:4324-4339.e8. doi:10.1016/j.molcel.2022.10.017.

Voeltz, G.K., E.M. Sawyer, G. Hajnóczky, and W.A. Prinz. 2024. Making the connection: How membrane contact sites have changed our view of organelle biology. *Cell*. 187:257–270. doi:10.1016/j.cell.2023.11.040.

Wang, C., B. Wang, T. Pandey, Y. Long, J. Zhang, F. Oh, J. Sima, R. Guo, Y. Liu, C. Zhang, S. Mukherjee, M. Bassik, W. Lin, H. Deng, G. Vale, J.G. McDonald, K. Shen, and D.K. Ma. 2022. A conserved megaprotein-based molecular bridge critical for lipid trafficking and cold resilience. *Nat Commun*. 13:6805. doi:10.1038/s41467-022-34450-y.

Wang, C.-W., J. Kim, W.-P. Huang, H. Abeliovich, P.E. Stromhaug, W.A. Dunn, and D.J. Klionsky. 2001. Apg2 Is a Novel Protein Required for the Cytoplasm to Vacuole Targeting, Autophagy, and Pexophagy Pathways *. *Journal of Biological Chemistry*. 276:30442–30451. doi:10.1074/jbc.M102342200.

Wang, X., P. Xu, A. Bentley-DeSousa, W. Hancock-Cerutti, S. Cai, B.T. Johnson, F. Tonelli, G. Talaia, D.R. Alessi, S.M. Ferguson, and P.D. Camilli. 2024a. Lysosome damage triggers acute formation of ER to lysosomes membrane tethers mediated by the bridge-like lipid transport protein VPS13C. 2024.06.08.598070. doi:10.1101/2024.06.08.598070.

Wang, Y., S. Dahmane, R. Ti, X. Mai, L. Zhu, L.-A. Carlson, and G. Stjepanovic. 2024b. Structural basis for lipid transfer by the ATG2A–ATG9A complex. *Nat Struct Mol Biol*. 1–13. doi:10.1038/s41594-024-01376-6.

Wang, Y., W. Huynh, T.D. Skokan, W. Lu, A. Weiss, and R.D. Vale. 2019. CRACR2a is a calcium-activated dynein adaptor protein that regulates endocytic traffic. *Journal of Cell Biology*. 218:1619–1633. doi:10.1083/jcb.201806097.

Wen, L., L. Liu, X. Shen, H. Li, Z. Zhu, H. Huang, M. Cai, D. Qian, S. Shen, Y. Qiu, Y. Cui, and Y. Sheng. 2020. The association of the UHRF1BP1 gene with systemic lupus erythematosus was replicated in a Han Chinese population from mainland China. *Annals of Human Genetics*. 84:221–228. doi:10.1111/ahg.12362.

Wirtz, K.W.A. 1991. Phospholipid transfer proteins: From lipid monolayers to cells. *Klin Wochenschr*. 69:105–111. doi:10.1007/BF01795953.

Wong, L.H., A.T. Gatta, and T.P. Levine. 2019. Lipid transfer proteins: the lipid commute via shuttles, bridges and tubes. *Nat Rev Mol Cell Biol*. 20:85–101. doi:10.1038/s41580-018-0071-5.

Xu, C.S., K.J. Hayworth, Z. Lu, P. Grob, A.M. Hassan, J.G. García-Cerdán, K.K. Niyogi, E. Nogales, R.J. Weinberg, and H.F. Hess. 2017. Enhanced FIB-SEM systems for large-volume 3D imaging. *eLife*. 6:e25916. doi:10.7554/eLife.25916.

Xu, C.S., S. Pang, G. Shtengel, A. Müller, A.T. Ritter, H.K. Hoffman, S. Takemura, Z. Lu, H.A. Pasolli, N. Iyer, J. Chung, D. Bennett, A.V. Weigel, M. Freeman, S.B. van Engelenburg,

1418 T.C. Walther, R.V. Farese, J. Lippincott-Schwartz, I. Mellman, M. Solimena, and H.F.
1419 Hess. 2021. An open-access volume electron microscopy atlas of whole cells and tissues.
1420 *Nature*. 599:147–151. doi:10.1038/s41586-021-03992-4.

1421 Yang, J., I. Anishchenko, H. Park, Z. Peng, S. Ovchinnikov, and D. Baker. 2020. Improved protein
1422 structure prediction using predicted interresidue orientations. *PNAS*. 117:1496–1503.
1423 doi:10.1073/pnas.1914677117.

1424 Yariv, B., E. Yariv, A. Kessel, G. Masrati, A.B. Chorin, E. Martz, I. Mayrose, T. Pupko, and N.
1425 Ben-Tal. 2023. Using evolutionary data to make sense of macromolecules with a "face-
1426 lifted" ConSurf. *Protein Science*. 32:e4582. doi:10.1002/pro.4582.

1427 Zhang, Y., W. Yang, C.C. Mok, T.M. Chan, R.W.S. Wong, M.Y. Mok, K.W. Lee, S.N. Wong,
1428 A.M.H. Leung, T.L. Lee, M.H.K. Ho, P.P.W. Lee, W.H.S. Wong, J. Yang, J. Zhang, C.-M.
1429 Wong, I.O.L. Ng, M.-M. Garcia-Barceló, S.S. Cherny, P.K.-H. Tam, P.C. Sham, C.S. Lau,
1430 and Y.L. Lau. 2011. Two missense variants in UHRF1BP1 are independently associated
1431 with systemic lupus erythematosus in Hong Kong Chinese. *Genes Immun*. 12:231–234.
1432 doi:10.1038/gene.2010.66.

1433

Figure 1

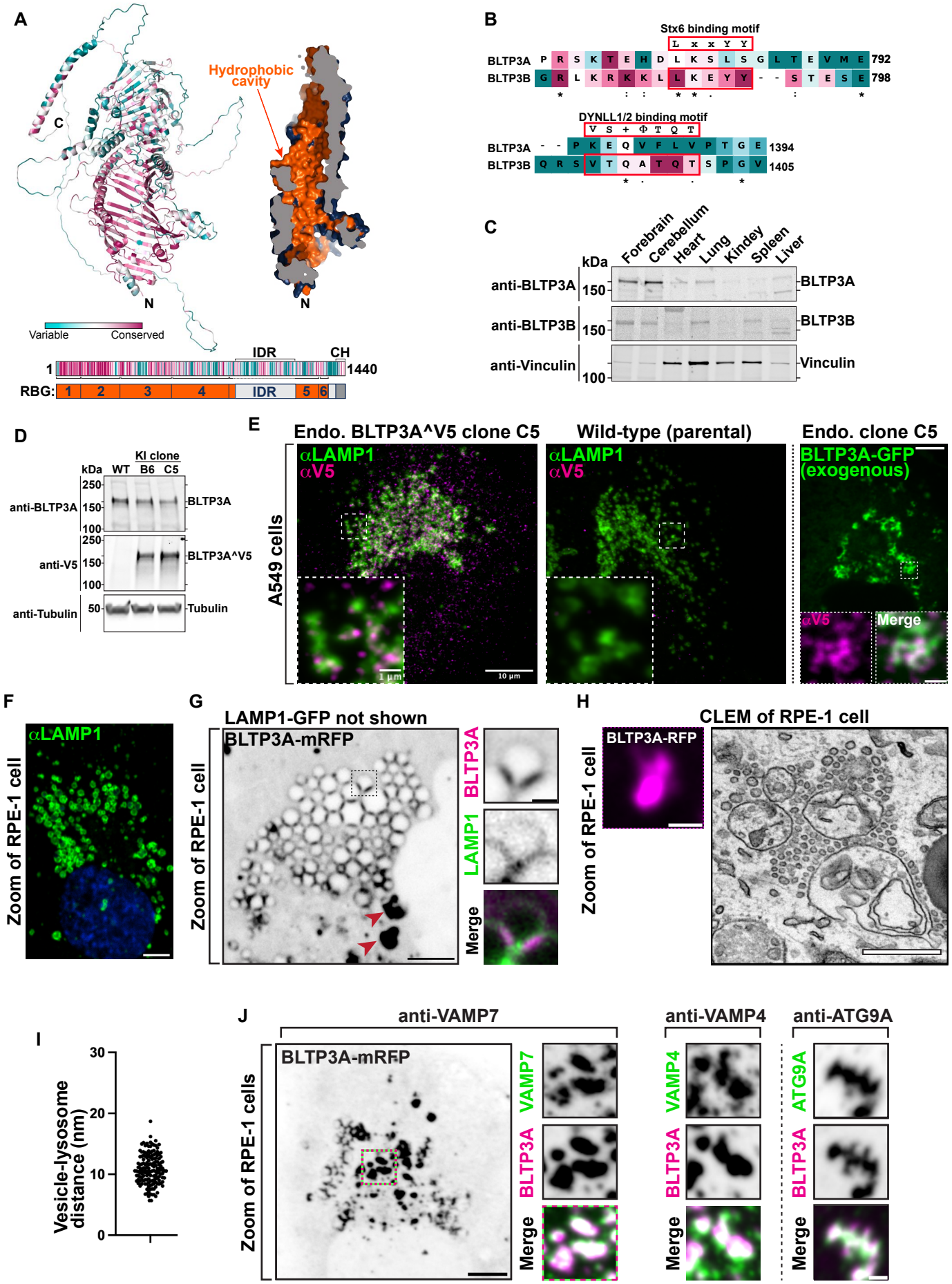
A
Hydrophobic cavity
C
N
N
Variable
Conserved
IDR
CH
1
1440
RBG:
1
2
3
4
IDR
5
6
B
Stx6 binding motif
L x x Y Y
BLTP3A P R S K T E H D L K S L S G L T E V M E 792
BLTP3B G R L K R K K L L K E Y Y - - S T E S E 798
DYNLL1/2 binding motif
V S + Φ T Q T
BLTP3A - - P K E Q V F L V P T G E 1394
BLTP3B Q R S V T Q A T Q T S P G V 1405
C
Forebrain
Cerebellum
Heart
Lung
Kindey
Spleen
Liver
kDa
anti-BLTP3A
150
BLTP3A
anti-BLTP3B
150
BLTP3B
anti-Vinculin
100
Vinculin
D
KI clone
kDa
WT
B6
C5
anti-BLTP3A
250
150
100
BLTP3A
anti-V5
250
150
100
BLTP3A^V5
anti-Tubulin
50
Tubulin
E
Endo. BLTP3A^V5 clone C5
Wild-type (parental)
Endo. clone C5
A549 cells
αLAMP1
αV5
αLAMP1
αV5
BLTP3A-GFP
(exogenous)
αV5
Merge
1 µm
10 µm
F
Zoom of RPE-1 cell
αLAMP1
G
LAMP1-GFP not shown
Zoom of RPE-1 cell
BLTP3A-mRFP
BLTP3A
LAMP1
Merge
H
CLEM of RPE-1 cell
Zoom of RPE-1 cell
BLTP3A-RFP
I
Vesicle-lysosome distance (nm)
30
20
10
0
J
anti-VAMP7
anti-VAMP4
anti-ATG9A
Zoom of RPE-1 cells
BLTP3A-mRFP
VAMP7
BLTP3A
Merge
VAMP4
BLTP3A
Merge
ATG9A
BLTP3A
Merge

Figure 2

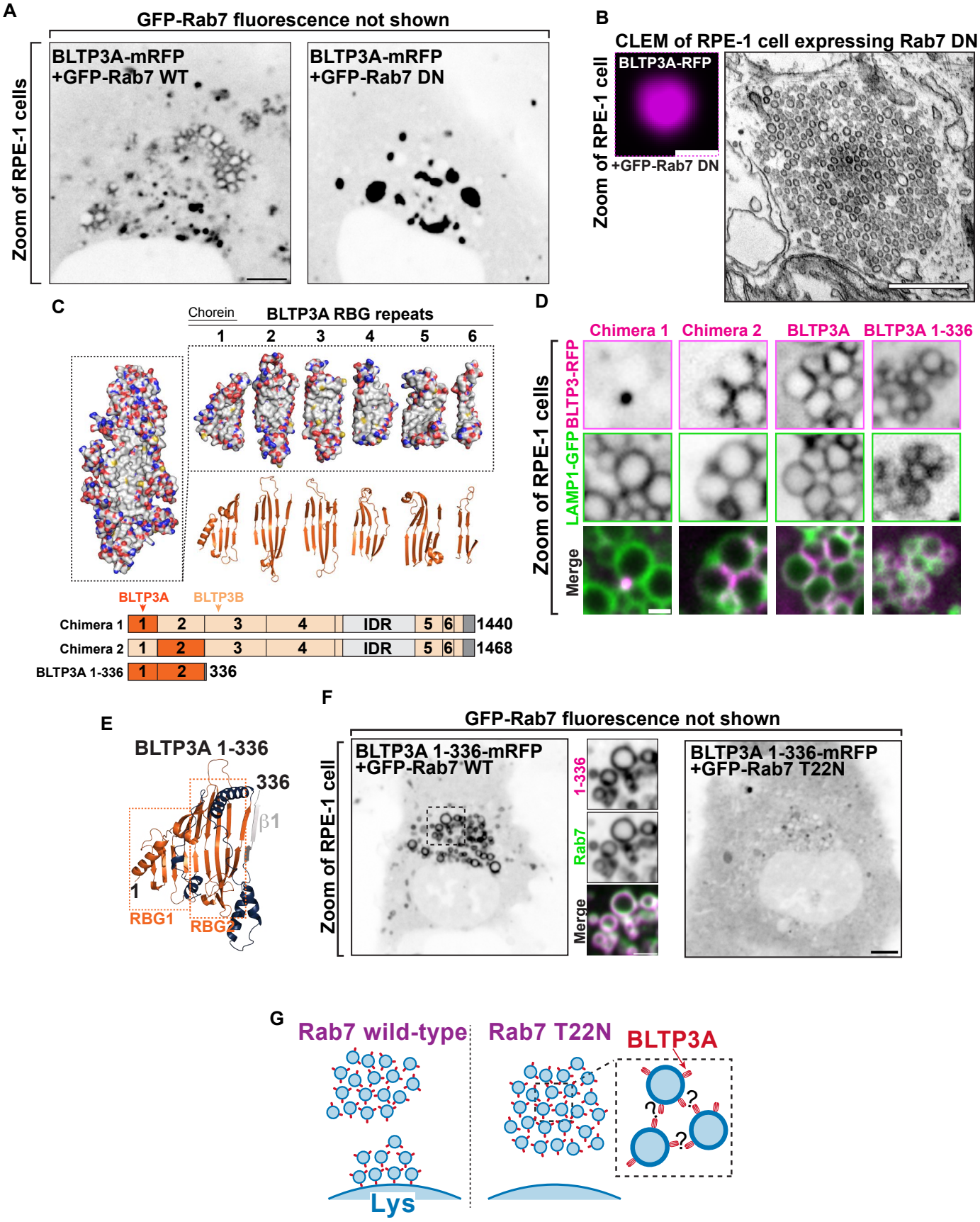
A
GFP-Rab7 fluorescence not shown
Zoom of RPE-1 cells
BLTP3A-mRFP
+GFP-Rab7 WT
BLTP3A-mRFP
+GFP-Rab7 DN
B
CLEM of RPE-1 cell expressing Rab7 DN
Zoom of RPE-1 cell
BLTP3A-RFP
+GFP-Rab7 DN
C
Chorein
BLTP3A RBG repeats
1 2 3 4 5 6
BLTP3A
BLTP3B
Chimera 1 1 2 3 4 IDR 5 6 1440
Chimera 2 1 2 3 4 IDR 5 6 1468
BLTP3A 1-336 1 2 336
D
Chimera 1
Chimera 2
BLTP3A
BLTP3A 1-336
Zoom of RPE-1 cells
BLTP3-RFP
LAMP1-GFP
Merge
E
BLTP3A 1-336
336
β1
1
RBG1
RBG2
F
GFP-Rab7 fluorescence not shown
Zoom of RPE-1 cell
BLTP3A 1-336-mRFP
+GFP-Rab7 WT
1-336
Rab7
Merge
BLTP3A 1-336-mRFP
+GFP-Rab7 T22N
G
Rab7 wild-type
Rab7 T22N
BLTP3A
Lys

Figure 3

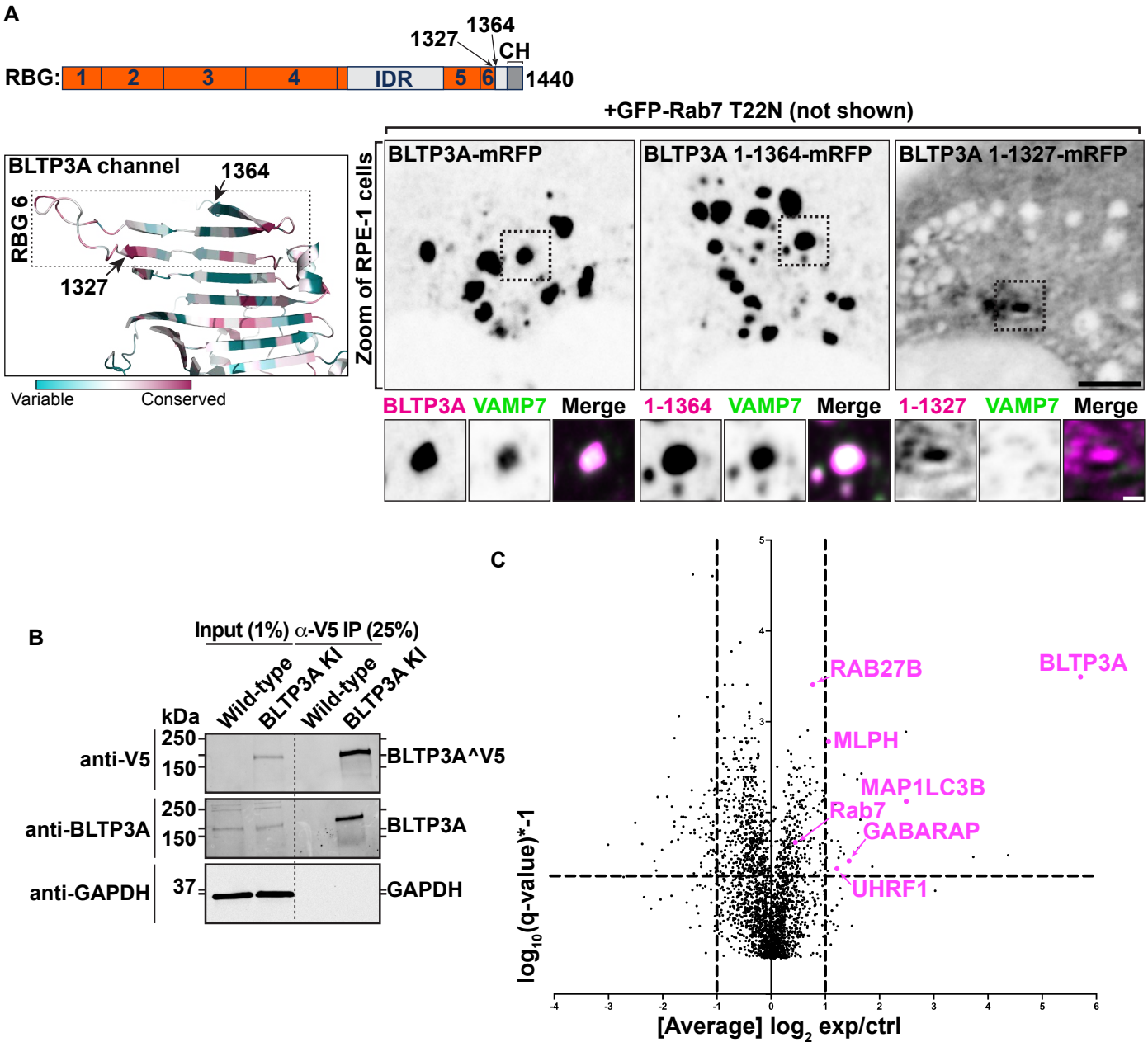
A
1327
1364
CH
RBG:
1
2
3
4
IDR
5
6
1440
+GFP-Rab7 T22N (not shown)
BLTP3A channel
1364
RBG 6
1327
Variable
Conserved
Zoom of RPE-1 cells
BLTP3A-mRFP
BLTP3A 1-1364-mRFP
BLTP3A 1-1327-mRFP
BLTP3A VAMP7 Merge
1-1364 VAMP7 Merge
1-1327 VAMP7 Merge
B
Input (1%) α-V5 IP (25%)
Wild-type
BLTP3A KI
Wild-type
BLTP3A KI
kDa
anti-V5
250
150
BLTP3A^V5
anti-BLTP3A
250
150
BLTP3A
anti-GAPDH
37
GAPDH
C
RAB27B
BLTP3A
MLPH
MAP1LC3B
Rab7
GABARAP
UHRF1
log10(q-value)*-1
[Average] log2 exp/ctrl

Figure 4

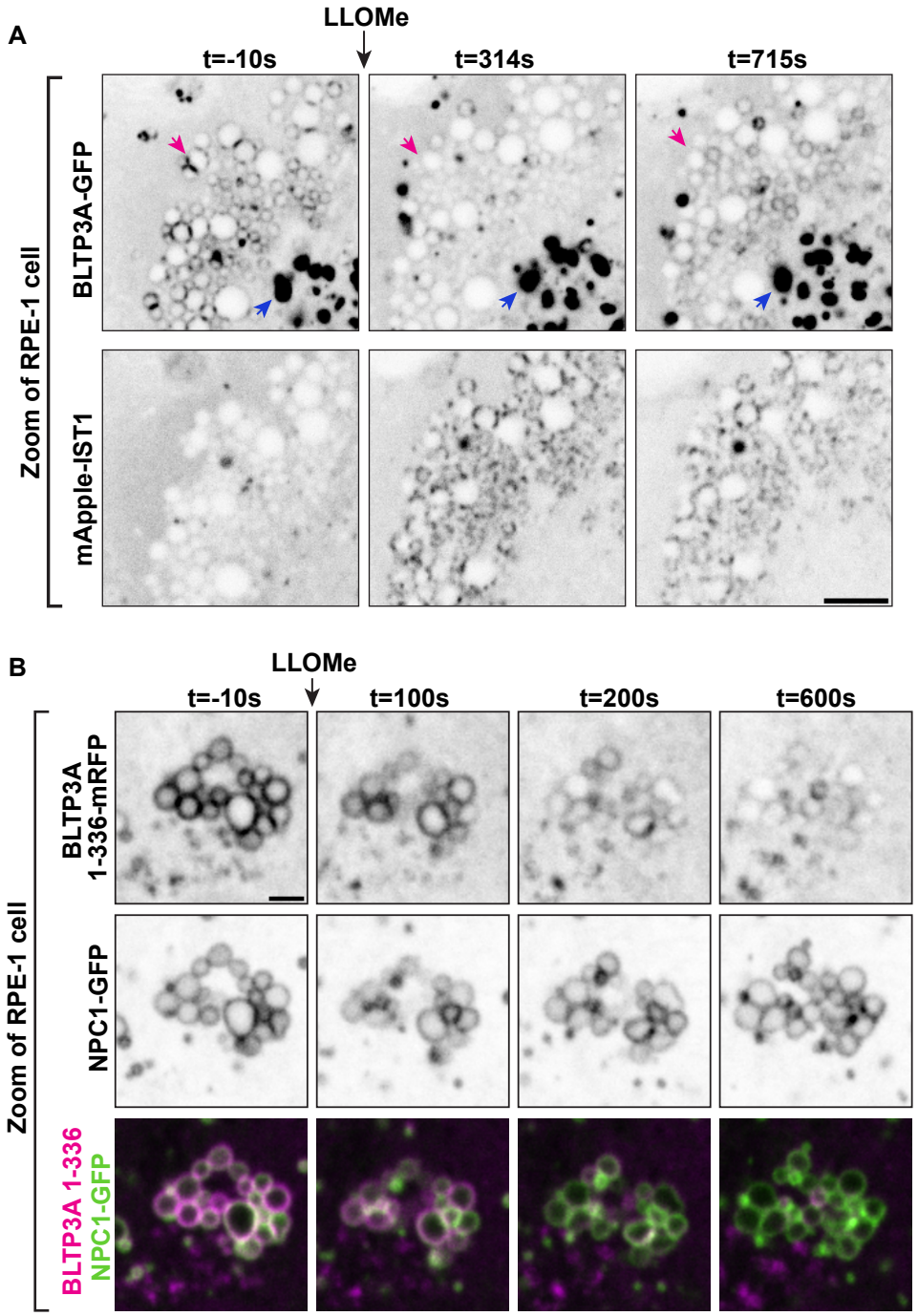
A
LLOMe
t=-10s
t=314s
t=715s
Zoom of RPE-1 cell
BLTP3A-GFP
mApple-IST1
B
LLOMe
t=-10s
t=100s
t=200s
t=600s
Zoom of RPE-1 cell
BLTP3A 1-336-mRFP
NPC1-GFP
BLTP3A 1-336
NPC1-GFP

Figure 5

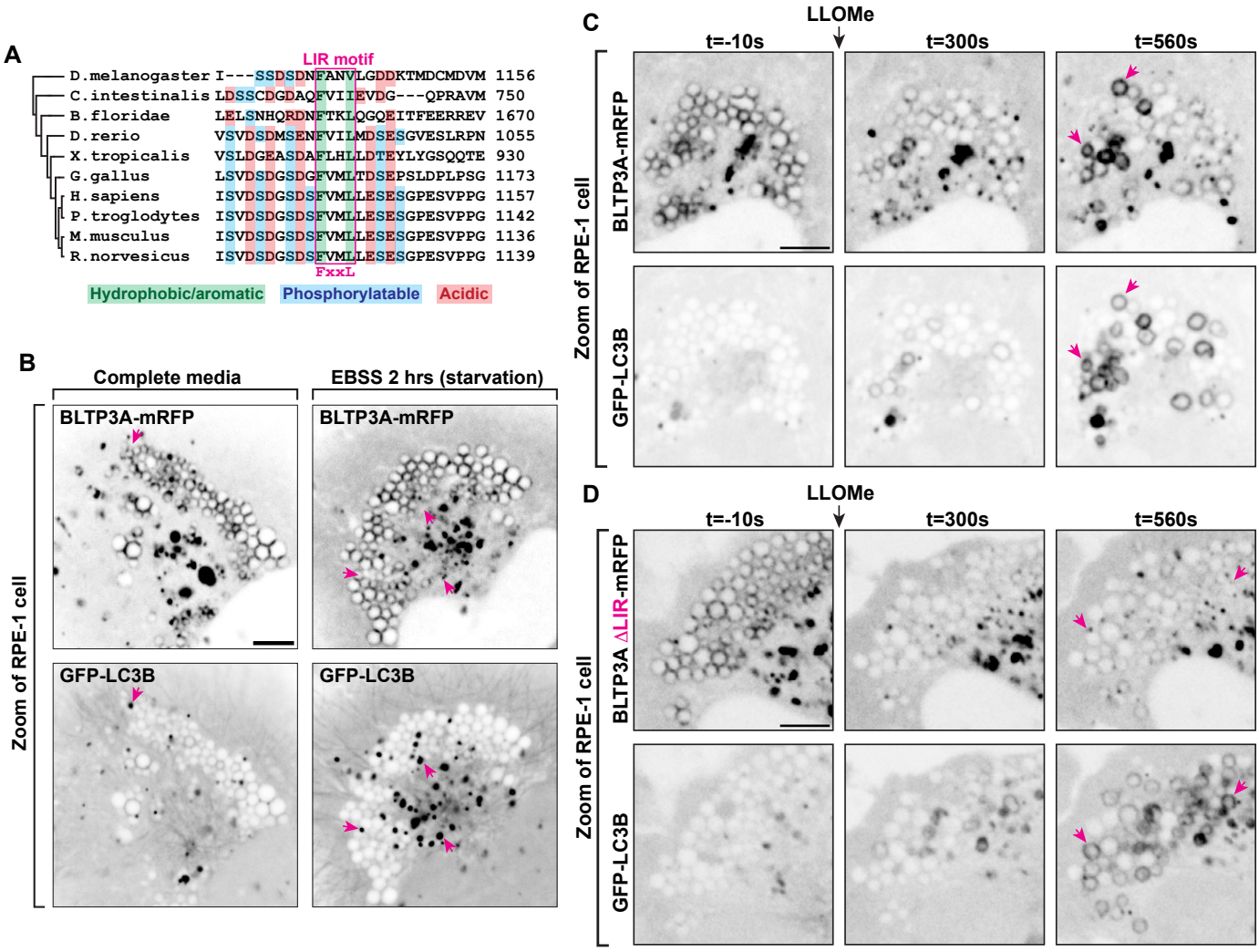
A
LIR motif
D.melanogaster I---SSDSDNFANVLGDDKTMDCMDVM 1156
C.intestinalis LDSSCDGDAQFVIIEVDG---QPRAVM 750
B.floridae LELSNHQRDNFTKLQGQEITFEERREV 1670
D.rerio VSVDSDMSENFVILMDSESGVESLRPN 1055
X.tropicalis VSLDGEASDAFLHLLDTEYLYGSQQTE 930
G.gallus LSVDSDGSDGFVMLTDSEPSLDPLPSG 1173
H.sapiens ISVDSDGSDSFVMLLESESGPESVPPG 1157
P.troglodytes ISVDSDGSDSFVMLLESESGPESVPPG 1142
M.musculus ISVDSDGSDSFVMLLESESGPESVPPG 1136
R.norvesicus ISVDSDGSDSFVMLLESESGPESVPPG 1139
FxxL
Hydrophobic/aromatic
Phosphorylatable
Acidic
B
Complete media
EBSS 2 hrs (starvation)
Zoom of RPE-1 cell
BLTP3A-mRFP
GFP-LC3B
C
LLOMe
t=-10s
t=300s
t=560s
Zoom of RPE-1 cell
BLTP3A-mRFP
GFP-LC3B
D
LLOMe
t=-10s
t=300s
t=560s
Zoom of RPE-1 cell
BLTP3A ΔLIR-mRFP
GFP-LC3B

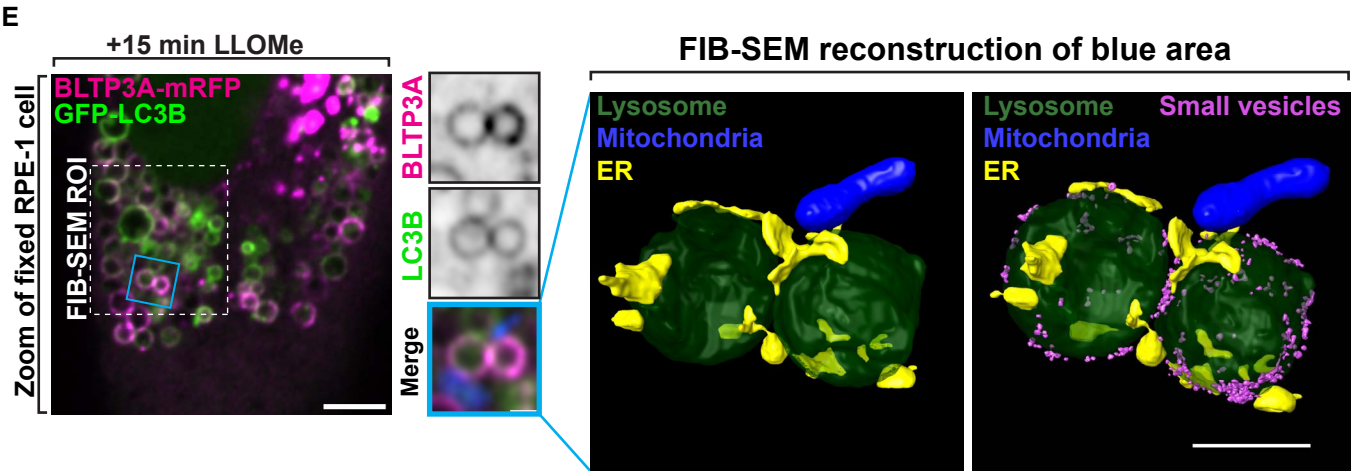
E
+15 min LLOMe
Zoom of fixed RPE-1 cell
BLTP3A-mRFP
GFP-LC3B
FIB-SEM ROI
BLTP3A
LC3B
Merge
FIB-SEM reconstruction of blue area
Lysosome
Mitochondria
ER
Lysosome
Small vesicles
Mitochondria
ER

Figure 6

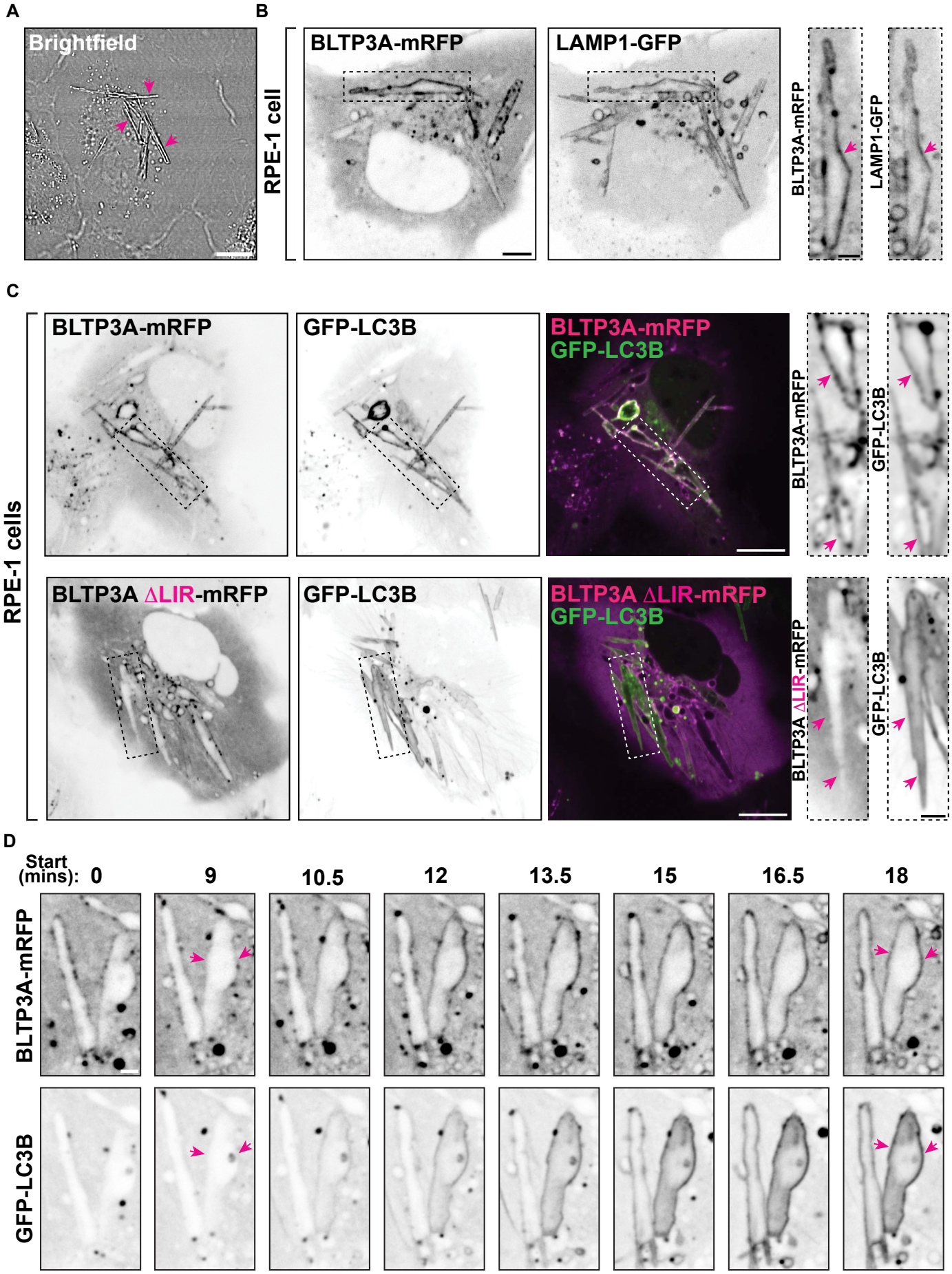
A
Brightfield
B
RPE-1 cell
BLTP3A-mRFP
LAMP1-GFP
BLTP3A-mRFP
LAMP1-GFP
C
RPE-1 cells
BLTP3A-mRFP
GFP-LC3B
BLTP3A-mRFP
GFP-LC3B
BLTP3A-mRFP
GFP-LC3B
BLTP3A ΔLIR-mRFP
GFP-LC3B
BLTP3A ΔLIR-mRFP
GFP-LC3B
BLTP3A ΔLIR-mRFP
GFP-LC3B
D
Start (mins): 0
9
10.5
12
13.5
15
16.5
18
BLTP3A-mRFP
GFP-LC3B

Figure 7

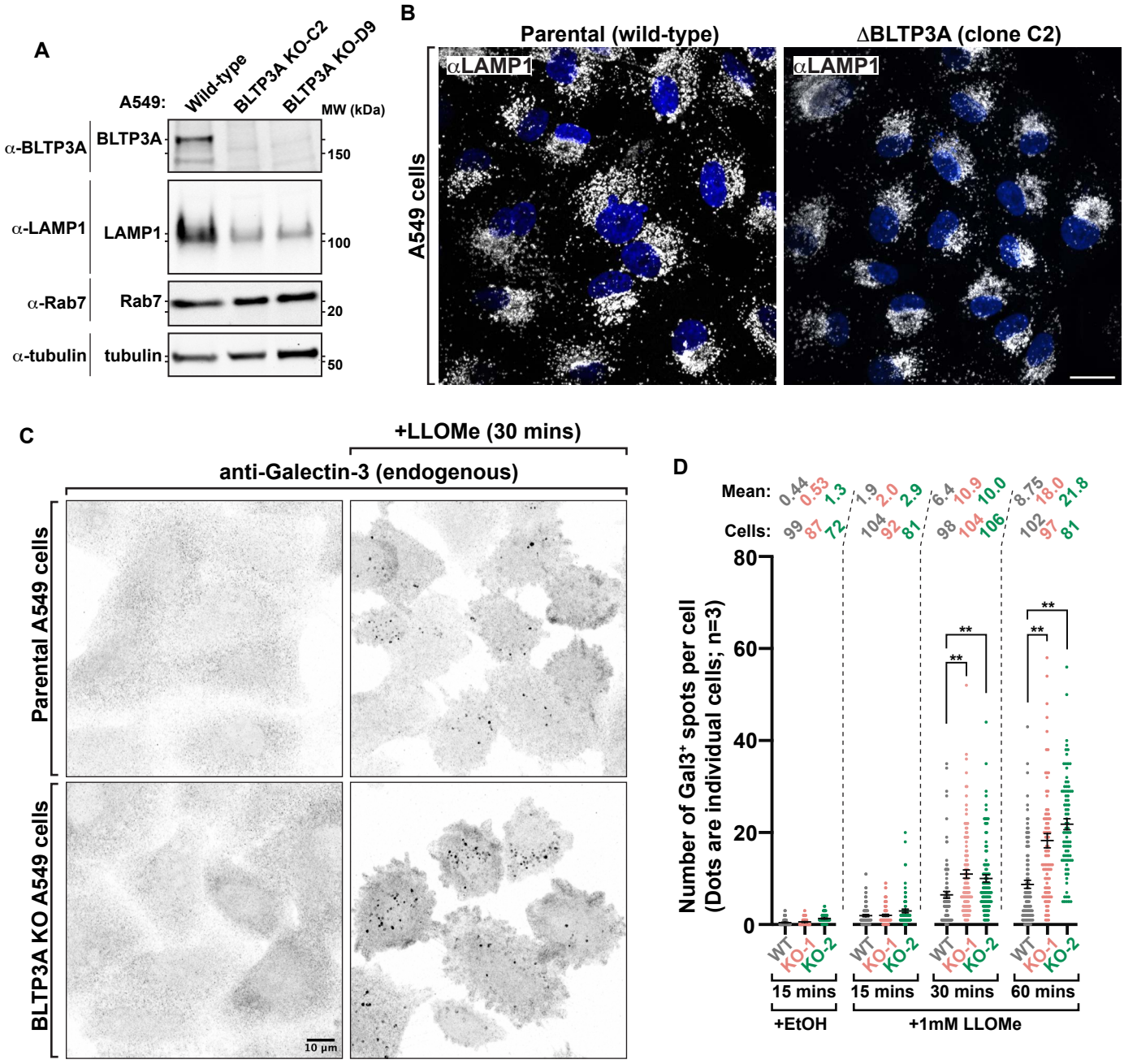
A
A549:
Wild-type
BLTP3A KO-C2
BLTP3A KO-D9
MW (kDa)
α-BLTP3A
BLTP3A
150
α-LAMP1
LAMP1
100
α-Rab7
Rab7
20
α-tubulin
tubulin
50
B
Parental (wild-type)
ΔBLTP3A (clone C2)
αLAMP1
αLAMP1
A549 cells
C
+LLOMe (30 mins)
anti-Galectin-3 (endogenous)
Parental A549 cells
BLTP3A KO A549 cells
10 µm
D
Mean: 0.44 0.53 1.3 1.9 2.0 2.9 6.4 10.9 10.0 8.75 18.0 21.8
Cells: 99 87 72 104 92 81 98 104 106 102 97 81
Number of Gal3⁺ spots per cell
(Dots are individual cells; n=3)
80
60
40
20
0
**
WT
KO-1
KO-2
15 mins
15 mins
30 mins
60 mins
+EtOH
+1mM LLOMe

Supplemental Figure 1

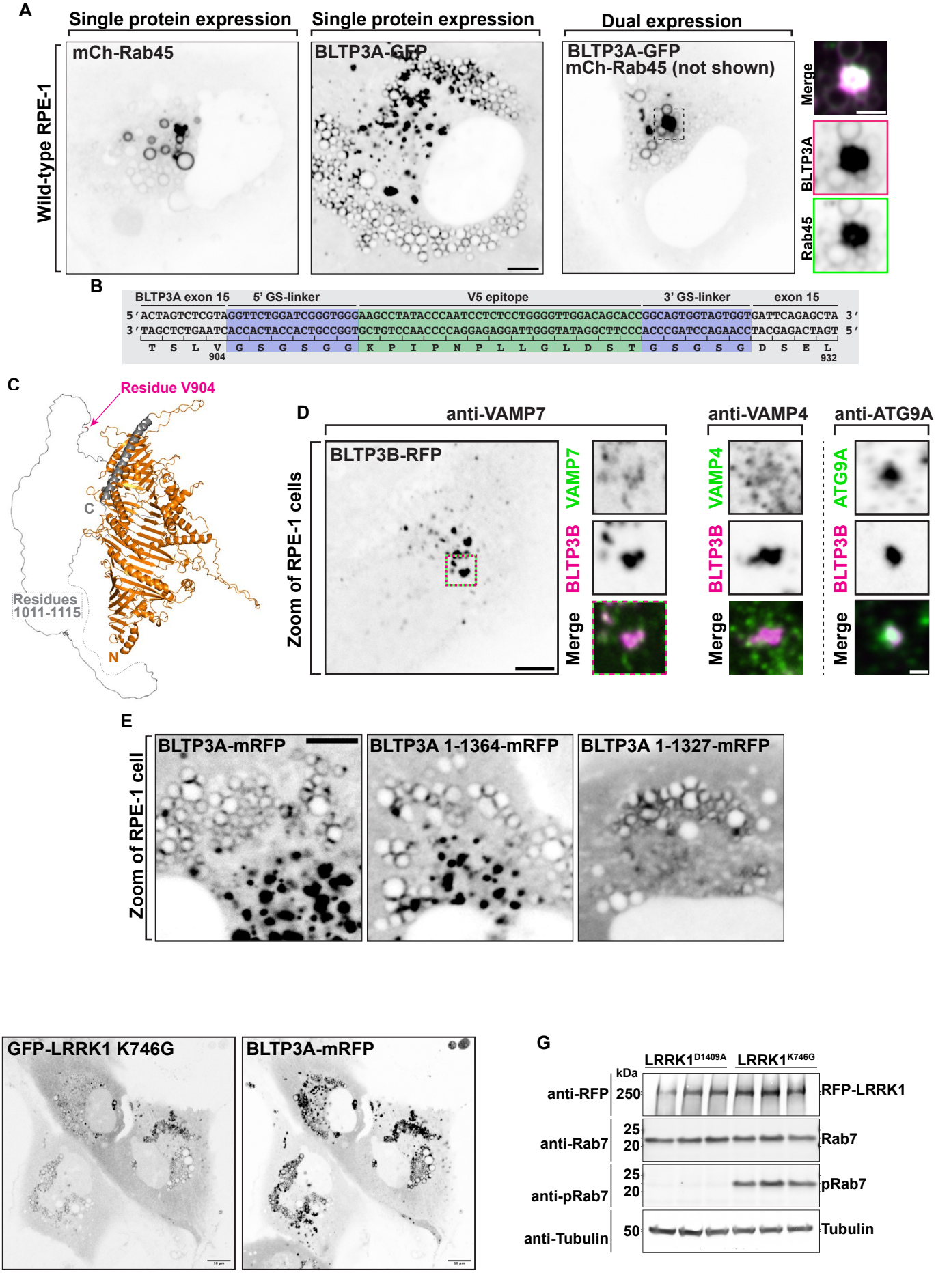

Supplemental Figure 2

A

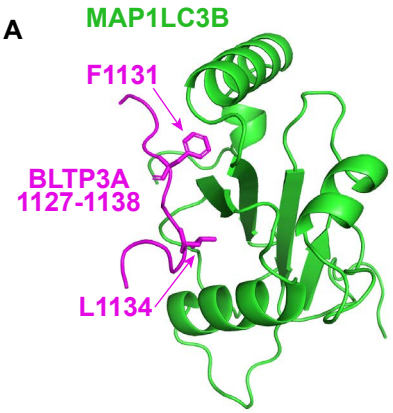

B

AF3 predictions of BLTP3A with mAtg8 proteins

BLTP3A:	1110-1150		1110-1150 ΔLIR	
	ipTM	pTM	ipTM	pTM
MAP1LC3A	0.66	0.7	0.31	0.69
MAP1LC3B	0.56	0.68	0.32	0.7
MAP1LC3C	0.57	0.62	0.32	0.62
GABARAP	0.74	0.76	0.55	0.74
GABARAPL1	0.73	0.75	0.52	0.72
GABARAPL2	0.72	0.74	0.53	0.73

C

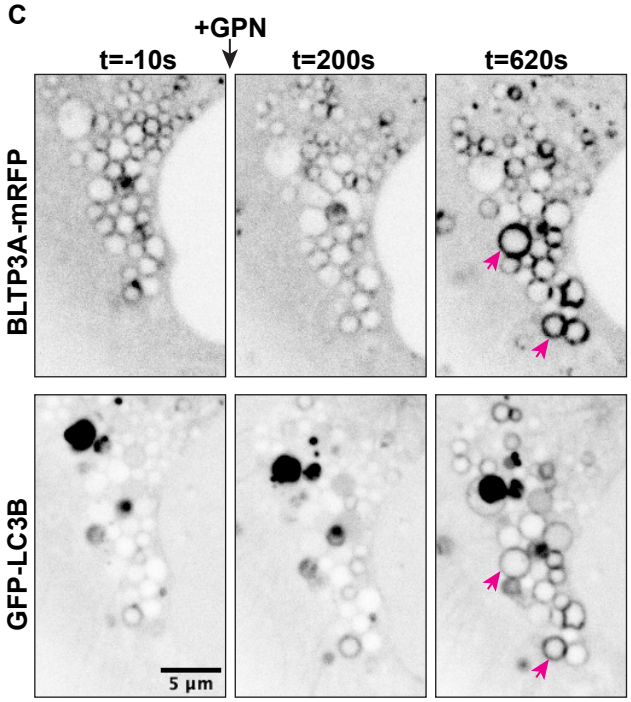

D
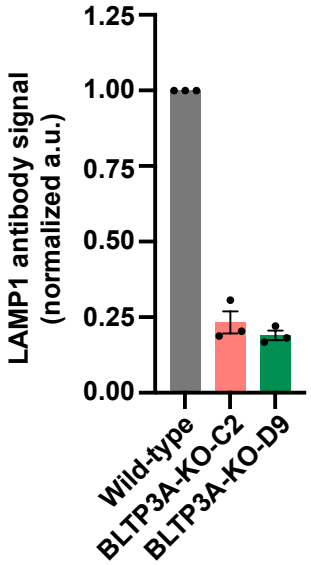
E